Title

Fully implantable and bioresorbable cardiac pacemakers without leads or batteries.

Journal

Nature Biotechnology, 39(10)

Authors

Choi, Yeon

Yin, Rose

Pfenniger, Anna

et al.

Publication Date

2021-10-01

DOI

10.1038/s41587-021-00948-x

Peer reviewed

Published in final edited form as:

Nat Biotechnol. 2021 October ; 39(10): 1228–1238. doi:10.1038/s41587-021-00948-x.

Fully implantable and bioresorbable cardiac pacemakers without leads or batteries

Yeon Sik Choi[1,2,3,24], **Rose T. Yin**[4,24], **Anna Pfenniger**[5,24], **Jahyun Koo**[1,2,24], **Raudel Avila**[6], **K. Benjamin Lee**[7], **Sheena W. Chen**[7], **Geumbee Lee**[1,2,3], **Gang Li**[8], **Yun Qiao**[4], **Alejandro Murillo-Berlioz**[9], **Alexi Kiss**[10,11], **Shuling Han**[12,13], **Seung Min Lee**[1], **Chenhang Li**[6], **Zhaoqian Xie**[14], **Yu-Yu Chen**[15], **Amy Burrell**[5], **Beth Geist**[5], **Hyoyoung Jeong**[1,2], **Joohee Kim**[1,2], **Hong-Joon Yoon**[1,2,3,16], **Anthony Banks**[1,2], **Seung-Kyun Kang**[17,18], **Zheng Jenny Zhang**[12,13], **Chad R. Haney**[19,20], **Alan Varteres Sahakian**[19,21], **David Johnson**[5], **Tatiana Efimova**[10,11], **Yonggang Huang**[1,3,6,22], **Gregory D. Trachiotis**[9], **Bradley P. Knight**[5], **Rishi K. Arora**[5,✉], **Igor R. Efimov**[4,✉], **John A. Rogers**[1,2,3,6,19,23,✉]

[1]Center for Bio-Integrated Electronics, Northwestern University, Evanston, IL, USA.

[2]Querrey Simpson Institute for Biotechnology, Northwestern University, Evanston, IL, USA.

[3]Department of Materials Science and Engineering, Northwestern University, Evanston, IL, USA.

[4]Department of Biomedical Engineering, The George Washington University, Washington, DC, USA.

[5]Feinberg School of Medicine, Cardiology, Northwestern University, Chicago, IL, USA.

✉**Correspondence and requests for materials** should be addressed to R.K.A., I.R.E. or J.A.R., r-arora@northwestern.edu; efimov@gwu.edu; jrogers@northwestern.edu.

Author contributions

Y.S.C., R.T.Y., A.P., J. Koo, R.K.A., I.R.E. and J.A.R. led the development of the concepts, designed the experiments and interpreted results. Y.S.C. and R.T.Y. led the experimental work with support from coauthors. R.T.Y., A.P., K.B.L., S.W.C., A.M.-B., S.H., A. Burrell, B.G. and R.K.A. performed in vivo surgery and associated pre-operative and post-operative procedures. R.T.Y., Y.Q. and G. Li performed ex vivo optical mapping. R.A., C.L., Z.X. and Y.H. performed computational modeling and simulations. R.K.A., I.R.E. and J.A.R. supervised the entire project. Y.S.C., R.T.Y., A.P., R.K.A., I.R.E. and J.A.R. wrote the paper. All authors read and approve the final manuscript.

Competing interests

The authors declare no competing interests.

online content

Any methods, additional references, Nature Research reporting summaries, source data, extended data, supplementary information, acknowledgements, peer review information; details of author contributions and competing interests; and statements of data and code availability are available at https://doi.org/10.1038/s41587-021-00948-x.

Code availability

The software for the analysis of optical mapping data, custom MATLAB software (RHYHTM) and custom scripts used in the study are freely available for download at https://github.com/optocardiography.

Additional information

Extended data is available for this paper at https://doi.org/10.1038/s41587-021-00948-x.

Supplementary information The online version contains supplementary material available at https://doi.org/10.1038/s41587-021-00948-x.

Peer review information *Nature Biotechnology* thanks the anonymous reviewers for their contribution to the peer review of this work.

[6]Department of Mechanical Engineering, Northwestern University, Evanston, IL, USA.

[7]Department of Surgery, The George Washington University, Washington, DC, USA.

[8]Center for Cardiovascular Research, Washington University School of Medicine, St. Louis, MO, USA.

[9]Department of Cardiothoracic Surgery, Veteran Affairs Medical Center, Washington, DC, USA.

[10]Department of Anatomy and Cell Biology, The George Washington University School of Medicine and Health Sciences, Washington, DC, USA.

[11]The George Washington Cancer Center, The George Washington University School of Medicine and Health Sciences, Washington, DC, USA.

[12]Comprehensive Transplant Center, Feinberg School of Medicine, Northwestern University, Chicago, IL, USA.

[13]Department of Surgery, Feinberg School of Medicine, Northwestern University, Chicago, IL, USA.

[14]State Key Laboratory of Structural Analysis for Industrial Equipment, Department of Engineering Mechanics, International Research Center for Computational Mechanics, Dalian University of Technology, Dalian, China.

[15]Materials Research Laboratory, University of Illinois at Urbana-Champaign, Urbana, IL, USA.

[16]School of Advanced Materials Science and Engineering, Sungkyunkwan University, Suwon, Republic of Korea.

[17]Department of Materials Science and Engineering, University of Illinois at Urbana-Champaign, Urbana, IL, USA.

[18]Frederick Seitz Materials Research Laboratory, University of Illinois at Urbana-Champaign, Urbana, IL, USA.

[19]Department of Biomedical Engineering, Northwestern University, Evanston, IL, USA.

[20]Center for Advanced Molecular Imaging, Northwestern University, Evanston, IL, USA.

[21]Department of Electrical and Computer Engineering, Northwestern University, Evanston, IL, USA.

[22]Department of Civil and Environmental Engineering, Northwestern University, Evanston, IL, USA.

[23]Department of Neurological Surgery, Feinberg School of Medicine, Northwestern University, Chicago, IL, USA.

[24]These authors contributed equally: Yeon Sik Choi, Rose T. Yin, Anna Pfenniger and Jahyun Koo.

Abstract

Temporary cardiac pacemakers used in periods of need during surgical recovery involve percutaneous leads and externalized hardware that carry risks of infection, constrain patient

mobility and may damage the heart during lead removal. Here we report a leadless, battery-free, fully implantable cardiac pacemaker for postoperative control of cardiac rate and rhythm that undergoes complete dissolution and clearance by natural biological processes after a defined operating timeframe. We show that these devices provide effective pacing of hearts of various sizes in mouse, rat, rabbit, canine and human cardiac models, with tailored geometries and operation timescales, powered by wireless energy transfer. This approach overcomes key disadvantages of traditional temporary pacing devices and may serve as the basis for the next generation of postoperative temporary pacing technology.

Implantable cardiac pacemakers are the cornerstones of therapy for bradyarrhythmias. As a complement to traditional pacemakers designed as permanent implants, temporary systems provide essential demand-based atrial and/or ventricular pacing for patients where bradyarrhythmias are expected to be short lived, such as on the order of days or weeks[1]. Such devices either act as a bridge to permanent pacing therapy[2] or are implemented temporarily following cardiac surgery[3] when postsurgical bradycardia is frequently encountered. Temporary pacing systems consist of an external generator with one or two transcutaneous pacing leads that are placed, depending on the clinical context, either epicardially or transvenously (Extended Data Fig. 1a). This hardware, however, carries substantial risk of complications. First, bacteria can form biofilms on foreign materials/devices such as pacing leads[4–8], and transcutaneous access can serve as a focus for infections[9–12]. Second, because the device is not fully implanted, the externalized power supply and control system can be inadvertently dislodged when caring for or mobilizing the patient. Third, removal of temporary transcutaneous devices following completion of therapy can cause laceration and perforation of the myocardium since the pacing leads can become enveloped in fibrotic tissue at the electrode–myocardium interface (Extended Data Fig. 1a)[13–15]. These circumstances create a unique need for an alternative temporary pacemaker technology that can deliver the necessary electrotherapy while addressing the associated physiological complications.

Here we present a fully bioresorbable, implantable, leadless cardiac pacemaker that operates in a battery-free fashion and is externally controlled and programmable. The device relies exclusively on materials that resorb when exposed to biofluids in a time-controlled manner via metabolic action and hydrolysis. The materials and design choices create a thin, flexible and lightweight form that maintains excellent biocompatibility and stable function throughout the desired period of use. Over a subsequent timeframe following the completion of therapy, the devices disappear completely through natural biological processes. Wireless energy transfer via resonant inductive coupling delivers power to the system in a manner that eliminates the need for batteries and allows for externalized control without transcutaneous leads. These characteristics, together with a miniaturized geometry, facilitate full implantation into the body to eliminate the need for percutaneous hardware, thereby minimizing the risk of device-associated infections and dislodgement. A set of systematic animal studies highlights aspects in bioresorbability, biocompatibility and electrical functionality of this type of temporary pacemaker technology. The device can effectively capture and sustain cardiac rhythms across different species and platforms, including human cardiac slices and mouse, rat, rabbit and canine hearts. Demonstrations

in mouse models illustrate capabilities in the treatment of atrioventricular (AV) nodal heart block, a common indication for pacemaker therapy. In vivo tests with canine models suggest the feasibility of this pacemaker system for adult human patients. Device implantation in rats highlights functionality for several days without degradation followed by complete resorption within 3 months. Taken together, these results establish the foundations for a bioresorbable electronics technology designed to address unmet needs in important areas of care for cardiac patients.

Results

Design of bioresorbable, battery-free cardiac pacemakers.

The schematic illustration in Fig. 1a (left) shows a thin, flexible, bioresorbable, leadless cardiac pacemaker on the surface of a heart. As part of the surgical implantation process, an integrated contact pad containing two dissolvable metallic electrodes (that is, bipolar channels) attaches to the myocardium. As shown in Fig. 1a (middle), the wireless power-harvesting part of the system includes a loop antenna with a bilayer, dual-coil configuration (tungsten-coated magnesium (W/Mg); thickness ~700 nm/~50 μm), a film of a poly(lactide-co-glycolide) (PLGA) 65:35 (lactide:glycolide) as a dielectric interlayer (thickness ~50 μm) and a radiofrequency (RF) PIN diode based on a doped monocrystalline silicon nanomembrane (Si NM; thickness ~320 nm). A strip of a double-layered electrode (W/Mg; thickness ~700 nm/~50 μm) with an opening at the end serves as an electrical extension and connector to deliver electrical stimuli from this receiver (Rx) antenna to the myocardium. This W/Mg electrode design enables compatibility with computed tomography (CT) for noninvasive monitoring of the bioresorption process. The layout of the PIN diode allows for a capacitor-free rectifier with high efficiency power transfer to the device (Supplementary Note 1). These two features represent key advancements over analogous peripheral nerve stimulators reported previously[16,17]. The pair of exposed electrodes (2.0 × 1.4 mm^2) includes adjacent holes (diameter 700 μm) as points for fixation to the heart with bioresorbable suture (Ethicon, no. MV-J451-V) (Fig. 1a, inset). A composite paste of Candelilla wax and W microparticles provides electrical interconnections[18]. Two layers of PLGA 65:35 define a top and bottom encapsulation (thickness 100 μm) structure around the entire system to isolate the active materials from the surrounding biofluids during the period of implantation. The entire system is small, thin (~0.05 ml; width ~16 mm; length >15 mm; thickness ~250 μm) and lightweight (~0.3 g) (Extended Data Fig. 2).

The key defining characteristic of this system is that all of the constituent materials are bioresorbable. The designs support stable function over a relevant timeframe with eventual complete disappearance into the surrounding biofluids and, eventually, from the body itself by natural chemical/biochemical processes of hydrolysis and metabolic action (Fig. 1a, right)[19]. For example, PLGA dissolves by hydrolysis into its monomers, glycolic and lactic acid[20]. The Mg, Si NM and W disappear into nontoxic products ($Mg + 2H_2O \rightarrow Mg(OH)_2 + H_2$), ($Si + 4H_2O \rightarrow Si(OH)_4 + 2H_2$) and ($2\,W + 2H_2O + 3O_2 \rightarrow 2H_2WO_4$), respectively[21–23]. Candelilla wax, which contains long-chain poly- and monounsaturated esters, fatty acids, anhydrides, short-chain hydrocarbons and resins, undergoes hydrolysis and resorbs into the body[18,24]. Figure 1b shows photographs of a typical bioresorbable

pacemaker at various time points following immersion in a PBS solution (pH 7.4) at physiological temperature (37 °C). The constituent materials largely dissolve within 5 weeks, and the remaining residues completely disappear after 7 weeks.

Figure 1c,d illustrates the proposed mode of use for this bioresorbable technology. Electrical stimulation is delivered by the implanted device to pace the heart at various rates, stimulation strengths and time periods by wireless power transfer according to the clinical need throughout the postoperative period (Fig. 1c). After resolution of bradycardia or insertion of a permanent device, temporary pacing is no longer necessary. Here, processes of bioresorption naturally eliminate the device completely without need for surgical extraction (Fig. 1d). Extended Data Fig. 1 compares the clinical implementation of current standard temporary pacemakers and the technology introduced here. The clinical device currently in use presents complications associated with external and percutaneous hardware, as well as the risk related to removal. In comparison, our device can be fully implanted because of its battery-free, leadless geometry, and it undergoes self-elimination by bioresorption.

Optimized mechanical layouts ensure conformal contact against the curved surface of the heart for effective and reliable pacing. Three-dimensional finite-element modeling (FEM) reveals distributions of principal strain for compression-induced buckling perpendicular to the length of the interconnects, as shown in Extended Data Fig. 3a. On the basis of the layouts and the mechanical moduli, the maximum strains in the Mg electrodes and PLGA encapsulation are <0.6% for a compression of 20%, corresponding to the linear elastic regime for each of these materials. Images of the device during twisting (180°) and bending (bend radius, 4 mm) highlight additional features of the flexible mechanics (Extended Data Fig. 3a–d). Wireless electrical measurements before and after twisting, compressing (that is, buckling) and bending show negligible differences in output voltage, consistent with expectations based both on FEM and analytical modeling results (Extended Data Fig. 3e).

Extended Data Fig. 4 summarizes the electromagnetic characteristics of the bioresorbable device for wireless and battery-free operation. Alternating currents (sine wave) generated by a function generator provide a source of monophasic RF power to a transmission (Tx) antenna (that is, primary coil) placed near the power harvester component of the device. The Rx coil (that is, secondary coil) transforms the received waveform to an approximately direct current output via the RF diode and delivers it to the interface with the myocardium (Extended Data Fig. 4a) as a cathodic direct current pulse through the electrode pads. An applied electrical stimulus above a threshold value initiates cardiac excitation as a result of depolarization of the transmembrane potential (that is, the difference in voltage between the inside and outside of the cell). This type of inductive scheme is common for wireless power transfer in implanted medical devices[25,26], because the magnetic coupling that occurs in this megahertz frequency regime (~13.5 MHz; Extended Data Fig. 4b,c,f) avoids absorption by biofluids or biological tissues[27]. Extended Data Fig. 4d,e illustrates the RF power (~7 peak-to-peak voltage (V_{pp}) at a 1-mm coupling distance) applied to the Tx antenna and the resultant monophasic output (13.2 V) at the contact pad.

Ex vivo electrical pacing in various cardiac systems.

Several ex vivo tests establish the operating features of the device and its efficacy in pacing. Three different cardiac systems with varying transmural thicknesses (mouse, ~0.7 mm; rabbit, ~5.0 mm; human, ~10 mm)[28–30] reflect the span of different impedances observed in human hearts depending on size and health status[31,32]. Finite-element analysis (FEA) simulations reveal electric field distributions near the electrode–myocardium interface following electrical stimulation (electrode spacing, 2 mm; applied voltage, 0.75 V) in three-dimensional (3D) and two-dimensional (*x*, *z* axes) space (Supplementary Fig. 2a,b, respectively). The results show that this bipolar electrode design induces a strong electric field in cardiac tissue and that different transmitting voltages and interelectrode distances influence the range—and therefore strength—of the electric field delivered by the pacemaker (Supplementary Fig. 2c). In practice, the desired operating point is at the minimum power that can pace the heart to minimize voltage-induced electroporation damage to the myocardium and to limit electrochemical degradation of the bioresorbable electrodes. For this reason, choices of electrode spacing (1–5 mm) depend on the impedance—and therefore the size—of the targeted cardiac tissue (Supplementary Note 2).

The images in Fig. 2a,d show the contact pads (electrode spacing, ~2 mm) of devices placed onto the anterior myocardium of ex vivo Langendorff-perfused mouse and rabbit hearts, respectively. Activation of the device by passing RF power (transmitting voltage, 1 V_{pp}) through a nearby Tx antenna (12-mm diameter; three turns) generates cathodal impulses sufficient to initiate pacing. Far-field electrocardiogram (ECG) recordings of mouse (Fig. 2b) and rabbit (Fig. 2e) hearts show a transition from narrow QRS complexes to widened, high-amplitude complexes consistent with ventricular capture by the pacemaker. Optical mapping yields action potential maps (Fig. 2c,f) that show anisotropic activation of the membrane potential originating from the site of placement of the electrode pad that clearly propagates throughout the ventricular myocardium, as expected (Supplementary Video 1). Supplementary Fig. 4 summarizes optical action potentials and activation map data obtained from pacing a mouse heart at different rates. The results indicate effective ventricular capture across a range of frequencies. Figure 2g shows a human ventricular heart slice (thickness, ~400 μm) in a constant-flow, temperature-controlled perfusion system. These optical action potentials and activation maps demonstrate successful pacing and activation of human cardiac tissue (Fig. 2h,i). Taken together, these ex vivo tests indicate that this bioresorbable, leadless, battery-free cardiac pacemaker technology is readily applicable across a size range of mammalian cardiac tissues, including the human heart.

Treating AV block in an ex vivo mouse model.

High-grade AV block corresponds to an interruption in the transmission of an impulse from the atria to the ventricles due to an anatomical or functional impairment in the cardiac conduction system[33]. This intermittent or absent AV conduction can be transient or permanent. For the past six decades, electrical pacemakers have been critical in the treatment of patients with AV block. The bioresorbable, leadless cardiac pacemaker introduced here is an attractive potential alternative to conventional pacemakers for such patients, particularly if AV block appears transient. Figure 3a illustrates treatment of AV block with this type of device. The demonstration begins with ischemic reperfusion to induce

second-degree AV block in an ex vivo Langedorff-perfused mouse heart. Healthy hearts exhibit a 1:1 association between the P-wave (atrial depolarization) and QRS complex (ventricular depolarization). In the far-field ECG shown in Fig. 3b, the first and third P-waves are not followed by an associated QRS complex. This behavior is consistent with ventricular bradycardia arising from 2:1 conduction block between the atria and ventricles (Fig. 3b). Ventricular pacing using the bioresorbable pacemaker (transmitting voltage, 1 V_{pp}; frequency, 10 Hz) promptly generates widened, amplified QRS complexes at a normal mouse heart rate of 10 Hz (600 beats per minute (bpm)) in the ECG, which is consistent with effective ventricular pacing and prevention of bradycardia. Measurements of optical action potentials also confirm the efficacy for treatment of AV block. Figure 3c (left) shows placement of the electrodes on the myocardial surface relative to the position of the atria and ventricles during optical recording. The results in Fig. 3c (middle) clearly show the conduction block between the atria and ventricles, with 2:1 AV conduction. Electrical stimulation of the ventricles with the device restores ventricular activation that is critical for ventricular mechanical function and cardiac output. The activation map shows clear anisotropic activation originating from the contact electrode and propagation of the action potential throughout the entire ventricular myocardium (Fig. 3c, right), consistent with activation of the ventricles by the pacemaker.

Placing the electrode on the right atrium (RA) near the sinoatrial (SA) node enables electrical stimulation of the atria in a mode that closely matches the physiological conduction system of the heart for native AV conduction. The schematic illustration in Supplementary Fig. 5a shows the electrode pad of the bioresorbable pacemaker attached to the RA. ECG signals before and after electrical stimulation confirm capture of the P-wave (Supplementary Fig. 5b). This result indicates that atrial pacing also can drive the rhythm of the heart for treatment of AV block.

In vivo pacing in a large-animal model.

In vivo studies with a canine whole-heart model at a scale that recapitulates human physiology are of high relevance to the envisioned clinical implementation since the canine cardiovascular system bears high resemblance to that of a human. Here, in vivo testing in a canine model (adult hound dogs, female, 27–36 kg) during open-chest surgery demonstrates the feasibility of this bioresorbable, leadless, battery-free pacemaker in a large animal. The illustration in Fig. 4a shows the setup. Electrical pulses generated using a power and stimulation controller, including a waveform generator and amplifier, pass through a Tx coil to the Rx coil of the device. Using adhesive electrodes attacehd to the limbs, a six-lead ECG system monitors cardiac activity throughout the period of the experiments. The photographs in Fig. 4b show the device sutured to the myocardial surface of the right ventricle and the sutured incision after chest closure. Figure 4c presents ECG recordings of the intrinsic rhythm (plain background, ~120 bpm) and ventricular capture (shaded background, 200 bpm) with clear pacing spikes and ventricular pacing morphologies of the QRS complex after placing the Tx coil in proximity to the Rx coil. Figure 4d shows the applied voltage (top) to the contact electrode (that is, output voltage) and the corresponding ECG signal (bottom). Following cathodal stimulation (output voltage, 30 V; pulse width, 5 ms; burst period, 300 ms), capture occurs at the onset of the impulse (that is, the leading edge). Here,

a widened, high-amplitude QRS complex appears following the epicardial pacing stimulus, which indicates ventricular capture. A 50–60-ms latency exists between the ventricular pacing stimulus and the QRS complex, as well as a low-amplitude delta wave at the onset of each QRS complex (Fig. 4c). The latency indicates that it requires ~50 ms for epicardial excitation to cross the ventricular wall and engage the endocardial Purkinje system. The low-amplitude delta wave is also due to epicardial pacing. A delta wave represents pre-excitation where the ventricles are excited earlier than expected in the normal cardiac conduction pathway. Because we are performing epicardial pacing at a rate faster than the intrinsic sinus rhythm, overdrive epicardial pacing causes pre-excitation in the ventricles so that a delta wave inflection is seen at the onset of each QRS complex. Therefore, these observations of a 50–60-ms latency and a delta wave at the onset of each QRS complex confirm that the bioresorbable pacemaker is successfully delivering epicardial stimuli for pacing in a large-animal model.

The power transfer for device operation depends on mutual inductance between the Rx and Tx coils. This relationship is represented by $M = k\sqrt{L_{\mathrm{Tx}}L_{\mathrm{Rx}}}$, where individual coil inductances are L_{Rx} and L_{Tx}. The coupling coefficient k defines the linkage of the magnetic flux; its value mainly depends on the distance and relative angle between the coils[34,35]. Proper design choices ensure operation for average skin-to-heart distance in adult patients (parasternal, 32 ± 8 mm; apical, 31 ± 10 mm; subcostal, 71 ± 20 mm)[36]. Supplementary Fig. 6 shows the magnetic field strength distribution for the coupling between a planar spiral Rx coil (25-mm diameter) and a 3D spiral Tx coil (64-mm diameter, four turns, power 1 W). As the distance between the coils increases from 3 to 20 mm, the coupling coefficient decreases, which consequently lowers the strength of the magnetic field in the receiver coil, resulting in reduced output voltage (Extended Data Fig. 4g). According to Faraday's law of induction, the time rate of change of magnetic flux through the Rx coil scales with its enclosed area to induce an output voltage. Thus, Rx coils of diameter <25 mm fail to meet the thresholds for output voltage required for pacing the canine heart at 20 mm (Fig. 4e). Magnetic field strength increases with the square root of the transmitting power. The use of increased power (2–12 W) and optimized (that is, larger area and high coupling coefficient) Rx and Tx coil geometries increase the working distance to >200 mm, as demonstrated by in vitro tests (Fig. 4f and Supplementary Fig. 8). In vivo pacing tests in a canine model validate the long-range wireless energy transfer capability of the bioresorbable pacing system. Here, the maximum pacing distance (that is, distance between skin and the Tx coil) is 17 cm, excluding the distance between the Rx coil and the skin (Fig. 4g, Supplementary Fig. 9 and Supplementary Note 3). Continuous pacing experiments in a fully equipped operation room for cardiac surgeries also confirm the absence of interference effects with standard electronic equipment either due to, or originating from, the wireless, bioresorbable pacing system (Supplementary Fig. 9c). The near-field (~13.56 MHz) wireless energy transfer mechanisms result in negligible changes in pacing signals during continuous operation with a skin-to-Tx coil distance of 10 cm. Overall, these in vivo tests suggest that the wireless power transfer system employed in the canine model can achieve the power transfer necessary for operation of bioresorbable pacemakers in adult human patients (clinical case scenario provided in Supplementary Note 4).

Chronic pacing capability.

Figure 5a summarizes the surgical procedure for implantation of a bioresorbable, leadless pacemaker in a small-animal (rat) model for chronic studies. Here, the pacemaker inserts through an incision in the intercostal space to access the thoracic cavity and interface to the ventricles of the heart. The Rx part of the system remains in the subcutaneous space. The electrode pads laminate to the anterior myocardial surface of the left ventricle and are secured by suture. The operation relies on a Tx antenna (12-mm diameter, three turns) that is applied and activated before and after closure of the chest to confirm proper function and placement. Continuous, user-controlled operation occurs through an RF powering system (Fig. 5b) and a large antenna that provides coverage throughout a location of interest (for example, the home cage or testing arena) at field strengths below Institute of Electrical and Electronics Engineers and Federal Communications Commission (FCC) guidelines[37]. Here, the RF system (that is, power and stimulation controller) connects to two Tx loop antennae outfitted on the outer surface of a plastic cage to deliver power to the implanted device (Supplementary Fig. 10). This RF setup, with an input power of 2 W (input frequency, 13.56 MHz), provides output voltages that exceed the threshold for pacing (~1 V at load resistance 5 kΩ) at any location (position and height) within the cage (Fig. 5c). Under these conditions, the specific absorption rate (SAR; a measure of the rate at which RF energy is absorbed by the body) remains below safety guidelines (Supplementary Fig. S11)[37].

Daily pacing trials were performed on all animals while they were awake or under light sedation using optimized parameters (transmitting power, ~6 W; pulse width, 7 ms; heart rate, 400–430 bpm). Data acquisition hardware monitors the ECG signal through subdermal needle electrodes positioned in the Lead I configuration (positive electrode on the right foreleg, negative electrode on the left foreleg, ground electrode on the hind leg). As before, pacing induces a transition of ECG signals from a narrow QRS complex, consistent with normal rate sinus rhythm (350–400 bpm), to a widened, amplified QRS complex with a shortened R–R interval, consistent with a paced rhythm (400–450 bpm). This change in ECG signal morphology indicates successful ventricular capture (Fig. 5d, day 0). Trials with programmable pacing parameters (transmitting voltage, ~10 V_{pp}; pulse width, 7 ms; heart rate, 400–430–bpm) support the capability for long-term in vivo pacing (Fig. 5d). These studies rely on a small Tx antenna (12-mm diameter, three turns) to pace the animals during light sedation. The stimulation threshold (that is, minimum transmitting voltage for pacing) increases from 1 V_{pp} at a rate of 1–2 V_{pp} day^{-1} (Supplementary Fig. 12a). Successful operation of the device for pacing in this small-animal model extends to postoperative day 4 (Fig. 5d, day 4). At day 5, the energy delivered by the device is sufficiently strong to produce pacing spikes in the ECG but is insufficient to capture the ventricular myocardium (Supplementary Fig. 12b). At day 6, the device fails to pace the heart even at transmitting voltages >10 V_{pp}. The functional lifetime depends on the encapsulation materials and thicknesses, along with the overall device layout[17,38,39] (Supplementary Note 5). These features can be adjusted to meet requirements specific to each clinical case.

In vivo bioresorbability and biocompatibility.

Here, the processes of bioresorption can be monitored noninvasively and at high resolution using CT. Typically, bioresorbable Mg features have low visibility in CT image due to

the low radiocontrast of Mg[40]. However, as described previously, an additional coating of high-radiocontrast bioresorbable metal (W, thickness ~700 nm) on the Mg (thickness, ~50 μm) makes visualization possible. Since the rate of dissolution of W is much lower (96 nm day^{-1}) than that of Mg (7,200 nm day^{-1})[19], this thin coating allows imaging over a timeframe similar to that of the in vivo bioresorption of the device. Figure 6a presents the results of noninvasive monitoring of bioresorption, indicating the gradual resorption of the device to its complete disappearance from the CT image on week 7. Figure 6b confirms these bioresorption processes in rats. At 1 week after implantation the device maintains its shape, and the contact with the heart also remains intact. Some reduction in size occurs due to resorption, as seen in the image taken at 2 weeks, but the device maintains its connection to the heart. At 4 weeks, fibrotic tissue envelops the diminished Rx coil and extension electrode and the device completely decouples from the heart. This fibrotic tissue limits diffusive access of biofluids to the surface of the bioresorbable materials, thereby decreasing the rates of chemical reactions that lead to bioresorption[41–43]. Images of explanted devices at 1, 3, 5 and 7 weeks provide additional insights into the resorption of the implanted Rx coil over time (Supplementary Fig. 15). The device largely dissolves within 3 weeks, and the remaining residues completely disappear after 12 weeks. Overall, the structure of the pacemaker shrinks and collapses over time to resorb into the surrounding tissues and biofluids as a mechanism for self-elimination of the device.

Histological examination of myocardial tissue near the site of pacemaker attachment up to 6 weeks after implantation provides evidence for the biocompatibile nature of the device, its constituent materials and the products of their dissolution. At the 0-, 3- and 6-week endpoints after implantation, histological analysis using Masson's trichrome staining quantifies the volume of myocardium, fibrotic tissue and interstitial space in transmural ventricular tissue near the site of device attachment (Fig. 7a). Images of stained cross-sections reveal normal cardiac tissue structure with fibrosis restricted to the outer boundaries of the epicardium at the contact point of the device, as expected. Quantitative analysis reveals no significant changes in the composition of the myocardial wall 3 weeks after implantation ($P < 0.05$) (Fig. 7b). Tracking of the weights of the animals following implantation (Fig. 7c) shows immediate reductions postoperatively, as anticipated for any major surgery. Subsequently, weights normalize to preoperative values and gradually increase with time, also as expected. These results, taken together with previously reported findings, provide strong evidence of the biocompatibility of the system.

Echocardiograms yield real-time, dynamic outlines of the walls of the heart for measurement of myocardial morphology and various hemodynamic parameters. Echocardiograms collected at 0, 1 and 3 weeks after device implantation show no evidence of differences in ejection fraction (Fig. 7d) or other hemodynamic parameters (diastolic volume, diastolic diameter, fractional shortening, systolic volume, systolic diameter, cardiac output) (Supplementary Fig. 16) between these time points. The results indicate that the implanted device negligibly affects the native mechanical function of the heart. To assess the level of inflammation in the heart following open-chest surgery and pacemaker implantation, we employed immunohistochemistry to visualize the immunoreactivity of the panleukocyte marker CD45 in the myocardium at the 0- (control), 3- and 6-week endpoints (Supplementary Fig. 17). Quantification of CD45 immunoreactivity in transmural

ventricular tissue near the site of device attachment shows no significant difference in the frequency of $CD45^+$ cells after pacemaker implantation, which indicates that the pacemaker and associated implantation surgery do not provoke an inflammatory response.

The results of serology tests provide a comprehensive understanding of the health status of rats with implanted pacemakers as the devices resorb (Fig. 7e,f). Blood levels of enzymes and electrolytes, as indicators of organ-specific diseases, fall within the confidence intervals of control values. Specifically, normal levels of alanine aminotransferase, cholesterol and triglyceride, phosphorus and urea nitrogen, calcium, albumin and total proteins respectively indicate the absence of disorders in liver, heart, kidney, bone and nerve tissue, as well as good overall health. Taken together, these histologic, echocardiographic, immunohistochemical and serologic results illustrate that the implantation and resorption of our bioresorbable pacemaker do not impact the natural physiology of the body system.

Discussion

The studies reported here establish a bioresorbable, leadless class of temporary cardiac pacemaker and demonstrate its efficacy in a comprehensive series of small- and large-animal models. The material compositions and design choices support electrical performance characteristics necessary for temporary cardiac pacing applications in a thin, flexible platform. Timescales for stable operation and complete bioresorption can be tailored to specific therapeutic timelines. This miniaturized device receives power and control commands through wireless inductive power transfer. This scheme circumvents the need for batteries and their associated mass, physical bulk and hazardous constituent materials. These fully implanted devices also minimize complications associated with infections by eliminating any percutaneous hardware, and bypass requirements for secondary device removal by self-elimination through bioresorption. Although the application evaluated in this series of experiments primarily addresses the need for temporary leadless epicardial pacing, future versions have the potential for transvenous applications of temporary, leadless pacing in patients with AV block due to myocarditis, or antitachycardic pacing in patients with atrial fibrillation associated with cardiac surgery. Promising directions for future research also include the incorporation of multisite pacing capabilities using different RF frequencies, the introduction of stimulus-responsive materials for active control of the processes of degradation[44] and the integration of sensors for closed-loop operation.

Methods

Preparation of bioresorbable components and integration into leadless, battery-free cardiac pacemakers.

Laser cutting defined the Mg (thickness 50 μm, Solution Materials) RF coil structures on temporary substrates of poly(dimethylsiloxane) (PDMS, 9:1). A sputtered coating of W (thickness, 700 nm) deposited on the Mg coil improves contrast in CT images to allow for noninvasive imaging of the bioresorption process. The double-layered W/Mg RF coil was transferred onto a substrate of PLGA (65:35 lactide:glycolide, Sigma-Aldrich) to serve as a receiving antenna for the power-harvesting unit. Solid-state diffusion of boron (tube furnace at 1,050 °C with N_2 flow) and phosphorus (tube furnace at 1,000 °C with N_2 flow)

through a photolithographically defined mask of SiO_2 formed by plasma-enhanced chemical vapor deposition yielded PIN RF diodes with monocrystalline Si NMs derived from a Si-on-insulator wafer (top silicon, thickness ~320 nm, p-type; Soitec). Removal of buried oxide by immersion in hydrofluoric acid allowed the release and transfer printing of Si NMs onto a sacrificial layer of diluted poly(pyromellitic dianhydride co-4,4′-oxydianiline) (DPI, ~200 nm) on a film of poly(methyl methacrylate) (~300 nm) on a silicon wafer. Photolithographic patterning and reactive ion etching determined the lateral dimensions of the doped Si NMs for integration into the PIN diodes. Liftoff procedures applied with Mg deposited by electron beam evaporation (thickness, ~300 nm; Kurt J. Lesker Co.) defined the electrical contacts. Spin casting an overcoat of DPI and dry etching through the underlying DPI and poly(methyl methacrylate) to define an open-mesh layout, followed by immersion in acetone, released the PIN diodes and allowed their transfer on the PLGA substrate (thickness, ~50 μm). Oxygen-reactive ion etching removed the DPI layers during/after transfer printing. Finally, the bioresorbable components (RF coil and PIN diode) were collected on a PLGA substrate and electrically interconnected with a biodegradable conductive W paste[18]. Covering the coils with PLGA and stacking the system yielded a compact, double-coil structure with openings for interconnections. Finally, laser cutting a piece of Mg foil (thickness, 50 μm) into 150-μm-wide electrodes and embedding them in PLGA produced electrical extension to the pads for the cardiac tissue interface.

Electric field distribution in heart tissue.

Finite-element analysis was implemented on the commercial software COMSOL 5.2a using the electrical current module (AC/DC Module User's Guide) to determine the electric field distribution in heart tissue for voltages applied to Mg electrodes of thickness 50 μm. The partial differential equation for the current is

$$\nabla \cdot J = Q_j \tag{1}$$

where Q_j is the current source and J is the current defined as $J = \sigma E$. The electric field is given by $E = -\nabla V$, where σ is electric conductivity and V is electric potential in the electrode pads. The effective volume—that is, volume with an electric field >100 mV mm^{-1} (Fig. 2b,c)—was determined from a triple integral (volume integration) over heart tissue in the parametric study for electrode spacing (0.1–5.0 mm) and applied voltage (0.5–2.5 V). The electrode pads and heart tissue were modeled using four-node tetrahedral elements. Convergence tests on mesh size were performed to ensure accuracy. The total number of elements in the models was ~400,000. The material properties used in the simulation were $\varepsilon_{Mg} = 1$, $\sigma_{Mg} = 2.25 \times 10^7$ S m^{-1} for Mg and $\varepsilon_{heart} = 8 \times 10^6$, $\sigma_{heart} = 0.1$ S m^{-1} for heart tissue[45–47].

Simulation of mechanical characteristics.

Commercial FEA software (ABAQUS, Analysis User's Manual 2016) was used to study the mechanical behaviors of the flexible Mg electrodes after deformations of physiological relevance—that is, those associated with the surface of the heart. The electrode can undergo up to ~20% compression before strain in the metal layer reaches the yield strain (0.6%) and initiates plastic deformation (Extended Data Fig. 3). The PLGA was modeled by hexahedron

elements (C3D8R) while the thin Mg layer (50 μm) was modeled by shell elements (S4R). The minimal element size was 1/8 the width of the Mg wires (300 μm), which ensured convergence of the mesh and accuracy of the simulation results. The elastic modulus (E) and Poisson's ratio (ν) used in the analysis were E_{Mg} = 45 GPa, ν_{Mo} = 0.35, E_{PLGA} = 16 MPa and ν_{PLGA} = 0.5.

Electromagnetic simulation.

The commercial software package ANSYS HFSS (ANSYS) was used to perform electromagnetic FEA to (1) determine the inductance, Q factor and scattering parameters S_{11} and S_{21} of the bioresorbable implantable double-layer Rx coils of outer diameter 8, 12, 18 and 25 mm and their corresponding matching Tx coil of the same diameter; and (2) quantify the influence of Rx and Tx coil size on power transfer efficiency and output voltage. The receiver coils of outer diameter 8, 12, 18 and 25 mm are tuned to operate at a resonant frequency f of 17.3, 13.91, 8.03 and 4.24 MHz, respectively, where the Q factor is maximum (Extended Data Fig. 4b and Supplementary Fig. 7b). Lumped ports were used to obtain the scattering parameter S_{nm} (Supplementary Fig. 7a) and port impedance Z_{nm} of both the Rx and Tx coils. An adaptive mesh (tetrahedron elements) and a spherical radiation boundary (radius, 1,000 mm) were adopted to ensure computational accuracy. Inductance (L) and Q (Extended Data Fig. 4b and Supplementary Fig. 7b), were obtained for all coils as $L_n = \mathrm{Im}\{Z_{nn}\}/(2\pi f)$ and $Q_n = |\mathrm{Im}\{Z_{nn}\}/\mathrm{Re}\{Z_{nn}\}|$, where $\mathrm{Re}\{Z_{nn}\}$, $\mathrm{Im}\{Z_{nn}\}$ and f represent the real and imaginary parts of Z_{nm} and the working frequency, respectively. Power transfer efficiency η is related to the magnitude of the scattering parameter S_{21} as[48]

$$\eta = |S_{21}|^2 \times 100\% \tag{2}$$

and the output voltage V can be calculated as

$$V = \frac{S_{21} V_s}{2} \sqrt{\frac{R_L}{R_S}} \tag{3}$$

where V_s and R_s are the input voltage and resistance, respectively, at the source and R_L is the resistance of the load in the Rx coil. The relationship between power transfer efficiency and working distance was calculated for a separation of 1–30 mm (Supplementary Fig. 7d) between the Rx and Tx coils in all four scenarios; similarly, the relationship between output voltage/power and working distance obtained is shown in Fig. 4e,f. The dielectric constant (ε) and electrical conductivity (σ) used in the model are ε_{Mg} = 1, $\sigma_{Mg} = 2.25 \times 10^7$ S m^{-1} for Mg coil traces in the Rx coils; and ε_{Cu} = 1, $\sigma_{Cu} = 5.8 \times 10^7$ S m^{-1}, δ_{Cu} = 0 for Cu traces in the Tx coils. Lastly, SAR, a measure of RF energy absorption in the body, was calculated for a mouse with a 25-mm-diameter Rx implant in a plastic cage with a double-loop Cu wire (AWG 12) Tx antenna operating at 13.56 MHz (Supplementary Fig. 10). The simplified mouse mesh ellipsoid body with major (half) axes of 8, 14 and 52 mm (Supplementary Fig. 11) was used to demonstrate that SAR was well below the safety guidelines of RF exposure[37]. The parameters ε, σ and density (ρ) used in the mouse model are ε_{Mouse} = 40, σ_{Mouse} = 0.5 S m^{-1} and ρMouse = 1, 000 kg m^{-3}.

Animals.

All animal procedures were performed according to the ethical standards and protocols (mouse: A367; rat: A364; rabbit: A327) approved by The George Washington University Institutional Animal Care and Use Committee, and in compliance with suggestions from the panel of Euthanasia of the American Veterinary Medical Association and the National Institutes of Health Guide for the Care and Use of Laboratory Animals. Optical mapping was performed on ex vivo mouse (15–30 weeks old; C57BL/6 background strain; male and female; $n = 3$) and rabbit (12–24 months old; New Zealand strain; female; $n = 2$) hearts. For in vivo studies, adult male and female Sprague–Dawley rats were used ($n = 25$) (Hilltop Animals).

Preparation of mouse and rabbit hearts for optical mapping.

Mice were anesthetized with isoflurane vapors. Rabbits were anesthetized using a mixture of 50 mg kg^{-1} ketamine and 10 mg kg^{-1} xylazine. The following procedure was performed for both mouse and rabbit hearts: cessation of pain was confirmed by toe pinch, the heart was quickly excised, and the aorta was cannulated in cardioplegic solution. The heart was then placed in a constant-pressure Langendorff system where the perfused solution was a modified Tyrode's solution (128.2 mM NaCl, 4.7 mM KCl, 1.05 mM $MgCl_2$, 1.3 mM $CaCl_2$, 1.19 mM NaH_2PO_4, 20 mM $NaHCO_3$, 11.1 mM glucose), which was maintained at 37 °C and was bubbled with 95% O_2/5% CO_2. The pressure of the heart was maintained at 60–80 mmHg throughout the experiment. Far-field ECG signals were acquired by using LabChart software (ADInstruments) with two sensing electrodes and one ground electrode placed in the bath around the heart.

Preparation of human ventricular heart slices for optical mapping.

All tissue procurement, preparation and experiments were performed according to protocols approved by the Institutional Review Board (IRB) of The George Washington University and international guidelines for human welfare. Donor human hearts rejected for organ transplant were acquired from the Washington Regional Transplant Community as deidentified discarded tissue with approval from IRB of The George Washington University. Human ventricular heart slices were created according to methods previously described[49]. Heart slices were then transferred and placed in a system perfused with modified Tyrode's solution (140 nN NaCl, 4.5 mM KCl, 10 mM glucose, 10 mM HEPES, 1 mM $MgCl_2$, 1.8 mM $CaCl_2$ pH 7.4), which was maintained at 37 °C and was bubbled with O_2.

Optical mapping.

Optical mapping was performed as previously detailed[49]. In brief, the optical mapping methods involved the following: mechanical motion of the slice was arrested using blebbistatin (5–10 μM), an electromechanical uncoupler. The tissue was stained with di-4-ANEPPS (125 nM), a voltage-sensitive fluorescent dye, for optical mapping of voltage changes in the membrane potential. Signals were recorded at 1–2 kHz using a high-speed CMOS camera with a MICAM Ultima acquisition system (SciMedia). The electrode of the bioresorbable pacemaker was placed on top of the slice in the central area. Using a function generator, the frequency (~10 MHz) and stimulating duration (1–5 ms) were set

to match the settings of the device for wireless inductive power transfer. For mouse and rabbit hearts, capture of the heartbeat was verified by far-field ECG measurement and the spatiotemporal dynamics of the activation of the transmembrane potential were recorded by optical mapping. For induction of AV block in the mouse heart, ischemic reperfusion was performed until confirmation of second-degree AV block by ECG. For human heart slices, capture was verified by evoked optical action potentials.

Processing of data from optical mapping.

Optical signals were processed using custom MATLAB software (RHYTHM) that is freely available at https://github.com/optocardiography. Each pixel was spatially filtered with a 3 × 3 uniform average bin. A finite-impulse response filter was used to filter each temporal sequence with a cutoff frequency of 100 Hz. Baseline drift was removed using polynomial subtraction and signal magnitude was normalized. Activation times across the membrane were determined by the time at which the maximum positive change in voltage (dV/dt_{max}) occurred for the recorded optical action potentials.

Implantation of pacemakers in rats.

All procedures were performed under general anesthesia using inhaled isoflurane vapor (1–3%). Throughout surgery, ventilation for the rats was provided by a VentElite small-animal ventilator (Harvard Apparatus). The heart was exposed via left thoracotomy, and the pacemaker electrodes were implanted on the myocardial surface of the left ventricle using 6–0 non-absorbable monofilament polypropylene suture (Ethicon, 8705H). The pacemaker receiver was placed within the subcutaneous pocket on the ventral surface of the rat. The thoracic cavity and muscle were closed by using absorbable 4–0 PGA suture (Oasis, MV-J451-V), and subsequently the skin was closed by using non-absorbable 4–0 nylon suture (Oasis, MV-1629-V). Pacemakers were tested at the end of the procedure to verify their function and confirm adequate placement. Animals were then taken off general anesthesia and allowed to recover. Appropriate postoperative monitoring and care were provided following surgery. For analgesia, an intraperitoneal dose of buprenorphine (0.5–1.0 mg kg^{-1}) was administered before incision and once every 12 h for 48 h following surgery.

Chronic in vivo pacing.

Pacemakers in all animals were tested daily post-procedure. Each day, animals were anesthetized with inhaled isoflurane vapor (2–3%) The Tx antenna was placed parallel to the receiver of the implanted device, to power the pacemaker and pace the heart. The frequencies of pacing stimulation were adjusted such that stimulation frequency was greater than that of the intrinsic rhythm of the heart. Three-lead ECG was monitored by subdermal needle electrodes in the Lead I configuration (positive electrode on the right forelimb, negative electrode on the left forelimb, ground electrode on the hind leg) using a PowerLab data acquisition system with LabChart software (ADInstruments). The heart rate was calculated from the R–R interval associated with the ECG. Daily testing in the same manner continued until the pacemaker failed to capture the heart.

Wireless operation of the bioresorbable pacemaker.

A commercial RF system (Neurolux, Inc.) was used to wirelessly deliver power to the bioresorbable cardiac pacemaker for whole-heart stimulation. The system included the following: (1) a laptop with custom software (Neurolux, Inc.) to control and command the data center, (2) a power distribution control box to supply wireless power and communicate with the devices through interactive TTL inputs, (3) an antenna tuner box to maximize power transfer and match the impedance of the source and the antenna and (4) an enclosed cage with customizable loop antenna designs for in vivo operation of the devices.

Weight monitoring, Masson's trichrome staining and immunohistochemistry.

Devices were implanted in both male and female Sprague–Dawley adult rats. Animals were weighed every 3 days to monitor their weight post surgery ($n = 3–6$ independent animals). The hearts of animals without implanted devices (control) and those with device implanted for 3 and 6 weeks were analyzed ($n = 3$ biologically independent animals per group). Animals were euthanized using 5% isoflurane vapor at 2 ml min^{-1} oxygen flow with an EZ anesthesia machine (EZ Systems, Inc.) until loss of consciousness. Once cessation of pain was confirmed by toe pinch, the heart was excised for euthanasia by exsanguination. Excised hearts were immediately cannulated and retrograde perfused, first with cardioplegic solution and then with neutral-buffered formalin. After 24 h, the hearts were transferred to a 70% ethanol solution and embedded in paraffin. Cross-sections underwent either Masson's trichrome staining for assessment of fibrosis or immunohistochemical staining to visualize localization of $CD45^+$ in the myocardium.

For Masson's trichrome-stained samples, cross-sections of the anterior left ventricle were imaged at ×4 magnification using an EVOS XL light microscope (Thermo Fisher Scientific). A custom MATLAB code was used to quantify the percentage volume of myocytes, collagen and interstitial space in these images. The region of interest was selected along the left ventricular free wall near the site of device implantation. Color deconvolution was performed to identify pink, blue and white pixels, which represent myocytes, collagen and interstitial space, respectively. The percentage volume encompassed by each of these structures was quantified by calculating the relative number of pixels per color in the selected region of interest.

For immunohistochemistry, sections were stained using the peroxidase/avidin–biotin-complex method. Briefly, the procedure was performed as follows: sections were deparaffinized using xylene and dehydrated with an ethanol concentration gradient. Antigen retrieval was performed using citrate buffer (pH 6.0) in a pressure cooker for 10 min. Slides were washed three times with ultrapure deionized H_2O (3 min per wash). Endogenous peroxidase activity was blocked with BLOXALL solution (SP-6000, Vector Laboratories) for 10 min. Slides were again washed three times with ultrapure deionized H_2O (3 min per wash). Samples were blocked for a further 30 min with normal goat blocking buffer (PBS, 0.15% Triton X-100, 1% BSA, 3% goat serum (no. 005000121, Jackson ImmunoResearch)) and incubated with the CD45 primary antibody overnight at 4 °C (1:50; no. ab10558, Abcam). Next, the samples were washed once in PBS with 0.5% Triton X-100 and twice in PBS (3 min per wash). Slides were incubated at room temperature with a biotinylated goat

anti-rabbit IgG secondary antibody (1:500; no. 65–6140, Invitrogen) for 60 min and with an avidin–biotin complex (ABC) reagent (no. PK-6100, Vector Laboratories) for 30 min. Samples were rinsed three times in PBS (3 min per wash) before and after application of the ABC reagent. Chromogenic development was achieved using the DAB Peroxidase Substrate Kit (no. SK-4100, Vector Laboratories). Samples were counterstained with hematoxylin (no. 6765007, Thermo Scientific) for 10 min, rinsed with tap water until colorless and dehydrated in an increasing gradient of ethanol followed by xylene. Slides were mounted with DPX mountant (no. 13512, Electron Microscopy Sciences), and images near the site of pacemaker implantation were taken using a bright-field microscope (no. DMi8, Leica Microsystems) in a tiled manner at ×20 and ×40 magnification using the Leica Application Suite (LAX) X software (Leica Microsystems). $CD45^+$ cells were manually quantified in a blinded manner using ImageJ (v.2.1.0, National Institutes of Health). Each counted cell was marked so that no cell was counted twice. A custom MATLAB code quantified the myocardial volume in each image using color deconvolution and calculated the frequency of $CD45^+$ cells mm^{-2}. To determine statistical differences, a nonparametric Kruskal–Wallis one-way analysis of variance with Dunn's test for pairwise comparison was performed across each condition between the 0- (control), 3- and 6-week endpoints at a significance level of $P < 0.05$.

Evaluation of hematology and blood chemistry of rats.

All procedures followed protocols approved by The George Washington University Institution Animal Care and Use Committee (IACUC). Blood was collected from adult rats (female Sprague–Dawley, $n = 3$) with bioresorbable pacemakers implanted using the aforementioned surgical procedures. At 1-, 3-, 5- and 7-week endpoints, blood was collected from animals via the tail vein into K-EDTA and gel tubes for blood counts and blood chemistry tests, respectively. Charles River Laboratories conducted the assays.

In vivo canine model study.

Retired breeder female hound dogs (age 1.2–3.5 years, weight 27–36 kg) used in this study were maintained in accordance with the Guide for the Care and Use of Laboratory Animals published by the US National Institutes of Health (NIH Publication no. 85–23, revised 1996) as approved by the IACUC of Northwestern University. Before surgery, all animals were premedicated with acepromazine (0.01–0.02 mg kg^{-1}) and induced with propofol (3–7 mg kg^{-1}). General anesthesia (inhaled) was achieved with isoflurane (1–3%) after intubation. Adequacy of anesthesia was assessed by toe pinch and palpebral reflex. Surface electrodes were applied to the limbs, and continuous six-lead ECG was recorded at a sampling rate of 977 Hz (Prucka CardioLab). A lateral thoracotomy was performed, and the heart was exposed by pericardiectomy. The electrodes of implanted bioresorbable pacemakers were sutured to the myocardial surface of the right ventricle with 4–0 monofilament nonresorbable sutures. For in vivo long-range tests of wireless operation, the thoracotomy was closed in four layers (ribcage, deep fascia and muscles, subcutaneous tissue and skin). A chest tube was placed before closing. The chest was evacuated of air and fluid and the lungs re-expanded. The chest tube was clamped. The antenna was applied at various distances from the receiver, and the selected pacing cycle length was 30–60 ms shorter than the intrinsic ventricular cycle length. Effective ventricular capture was confirmed by surface

ECG. Upon finishing the in vivo portion of the study and after confirming a very deep plane of anesthesia, the heart was removed and euthanasia was achieved by exsanguination.

In vivo bioresorption study.

Rats were anesthetized during imaging with a preclinical microCT imaging system (nanoScan PET/CT, Mediso-USA). Data were acquired at ×2.2 magnification with <60-μm focal spot, 1 × 4 binning and 720 projection views over a full circle, using 70-kVp/240-μA and 300-ms exposure time. Projection data were reconstructed with a voxel size of 68 μm (in all directions) and using filtered (Butterworth filter) back-projection software from Mediso. Amira 2020.1 (FEI Co.) was used to segment the device and skeleton, followed by 3D rendering.

Statistical analysis.

Results are reported as mean ± 6 s.d., unless otherwise noted. Statistical analyses were performed using Statistical software (v.6.0, Statsoft) followed by a *t*-test. $*P < 0.05$, $**P < 0.01$, $***P < 0.001$. All experiments were performed with at least three biological replicates per condition. For quantitative histology and immunohistochemical analysis, significance in column comparisons was calculated with a nonparametric Kruskal–Wallis test in conjunction with Dunn's multiple comparison test at a significance level of $P < 0.05$. For echocardiography data, significance in column comparisons was calculated using a Friedman test in conjunction with Dunn's multiple comparison test at a significance level of $P < 0.05$.

Reporting Summary.

Further information on research design is available in the Nature Research Reporting Summary linked to this article.

Extended Data

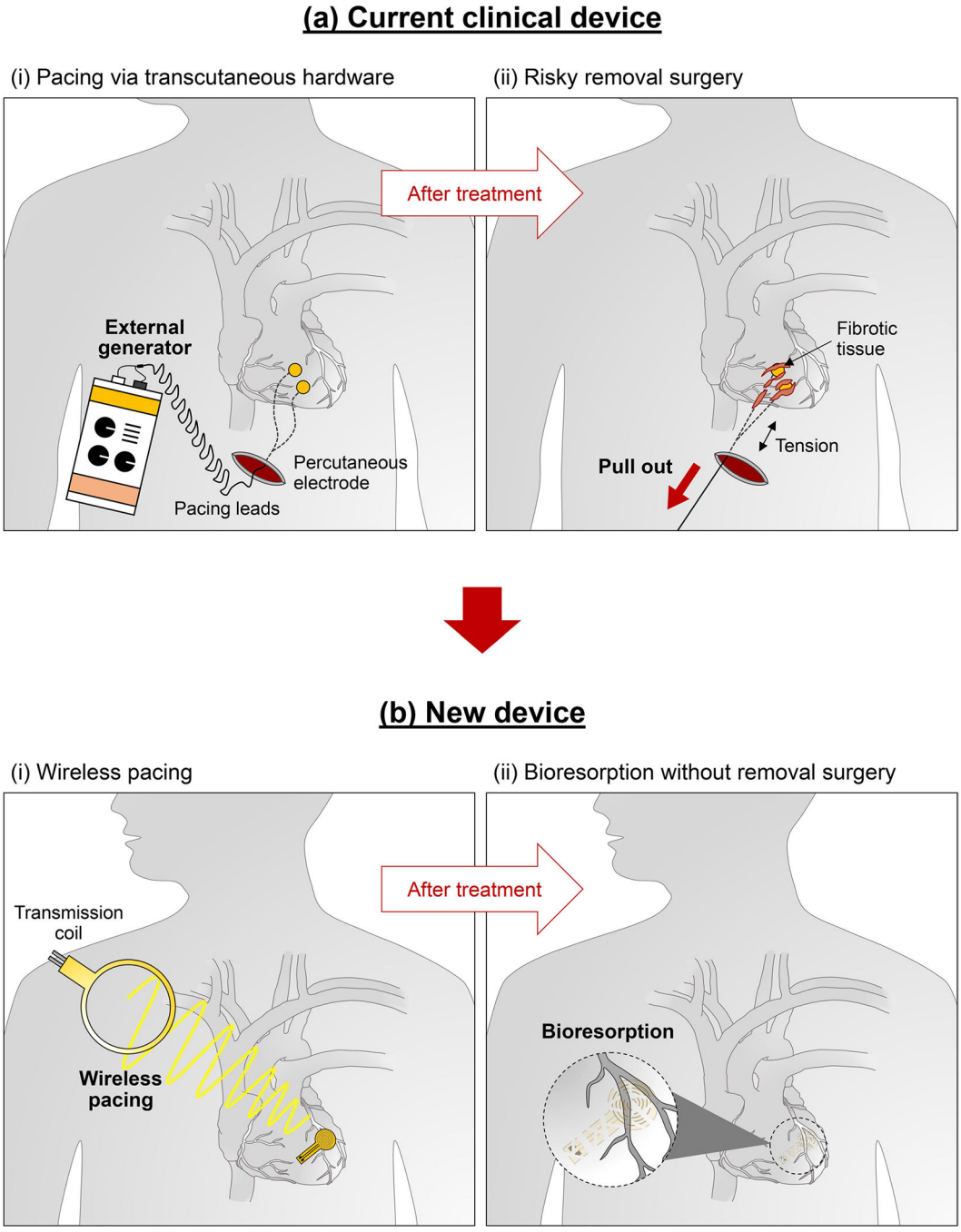

Extended Data Fig. 1 |. Illustrations that compare use scenarios of conventional temporary pacemakers and the bioresorbable, implantable, leadless, battery-free devices reported here. **a**, Schematic illustration that demonstrates the existing clinical approach for using conventional temporary pacemakers. (i) An external generator connects through wired, percutaneous interfaces to pacing electrodes attached to the myocardium. Temporary transvenous leads are affixed to the myocardium either passively with tines or actively with extendable/retractable screws. (ii) The pacing leads can become enveloped in fibrotic

tissue at the electrode-myocardium interface, which increases the risk of myocardial damage and perforation during lead removal. As a result, temporary epicardial leads placed at the time of open heart surgery are often cut and allowed to retract to avoid the risk of removal by traction. **b**, The proposed approach is uniquely enabled by the bioresorbable, leadless device introduced here. (i) Electrical stimulation paces the heart via inductive wireless power transfer, as needed throughout the post-operative period. (ii) Following resolution of pacing needs or insertion of a permanent device, the implanted device dissolves into the body, thereby eliminating the need for extraction.

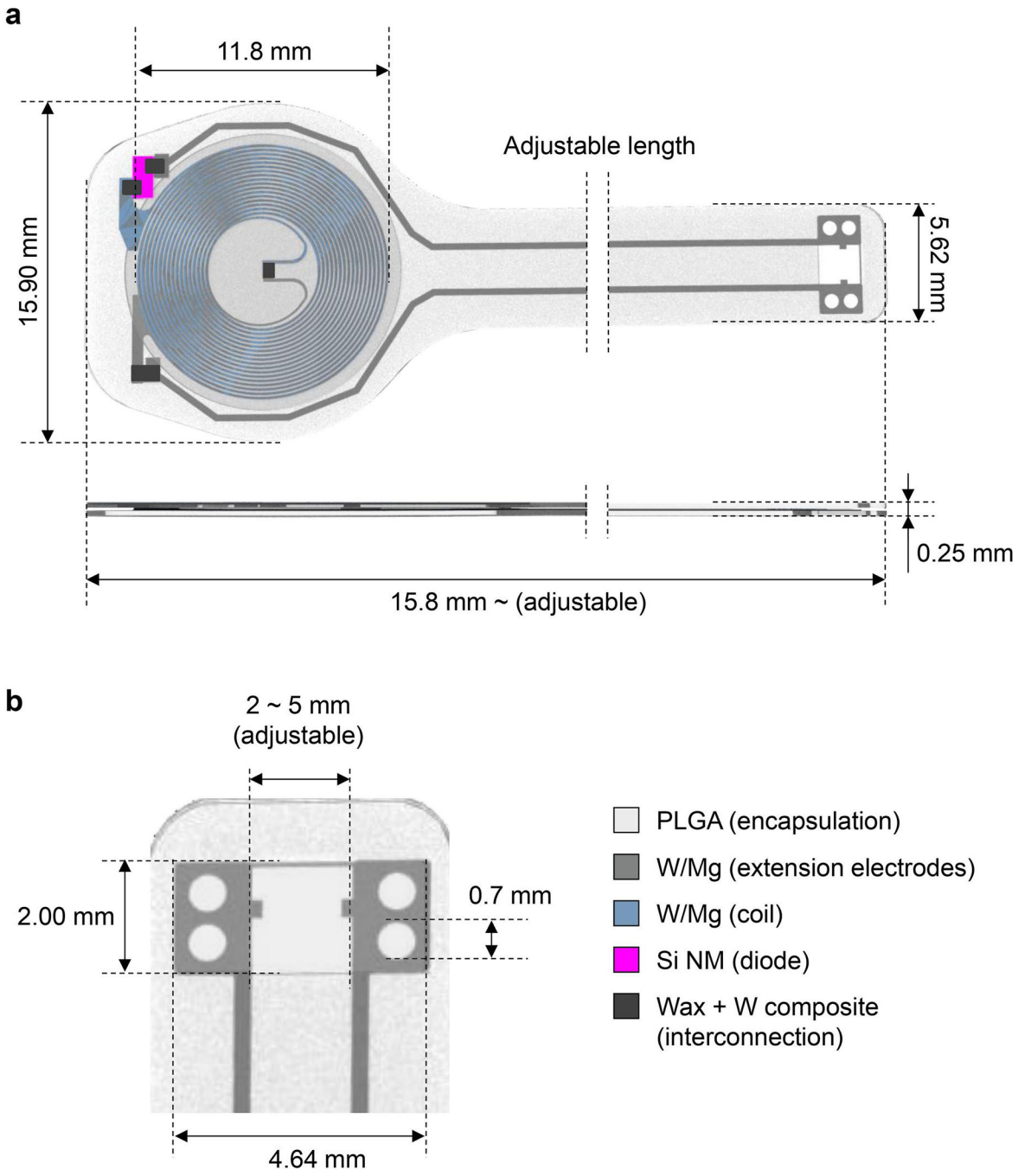

Extended Data Fig. 2 |. Design of bioresorbable, implantable, leadless, battery-free cardiac pacemaker.

a, Dimensions of the device: (top) x,y-view; (bottom) x,z-view. The minimum length of the device is 15.8 mm. The total length can be altered to meet requirements for the target application, simply by changing the length of the extension electrode. **b**, Dimensions of the contact pad. PLGA encapsulation covers the top surface of the contact electrode to leave only the bottom of contact electrode exposed.

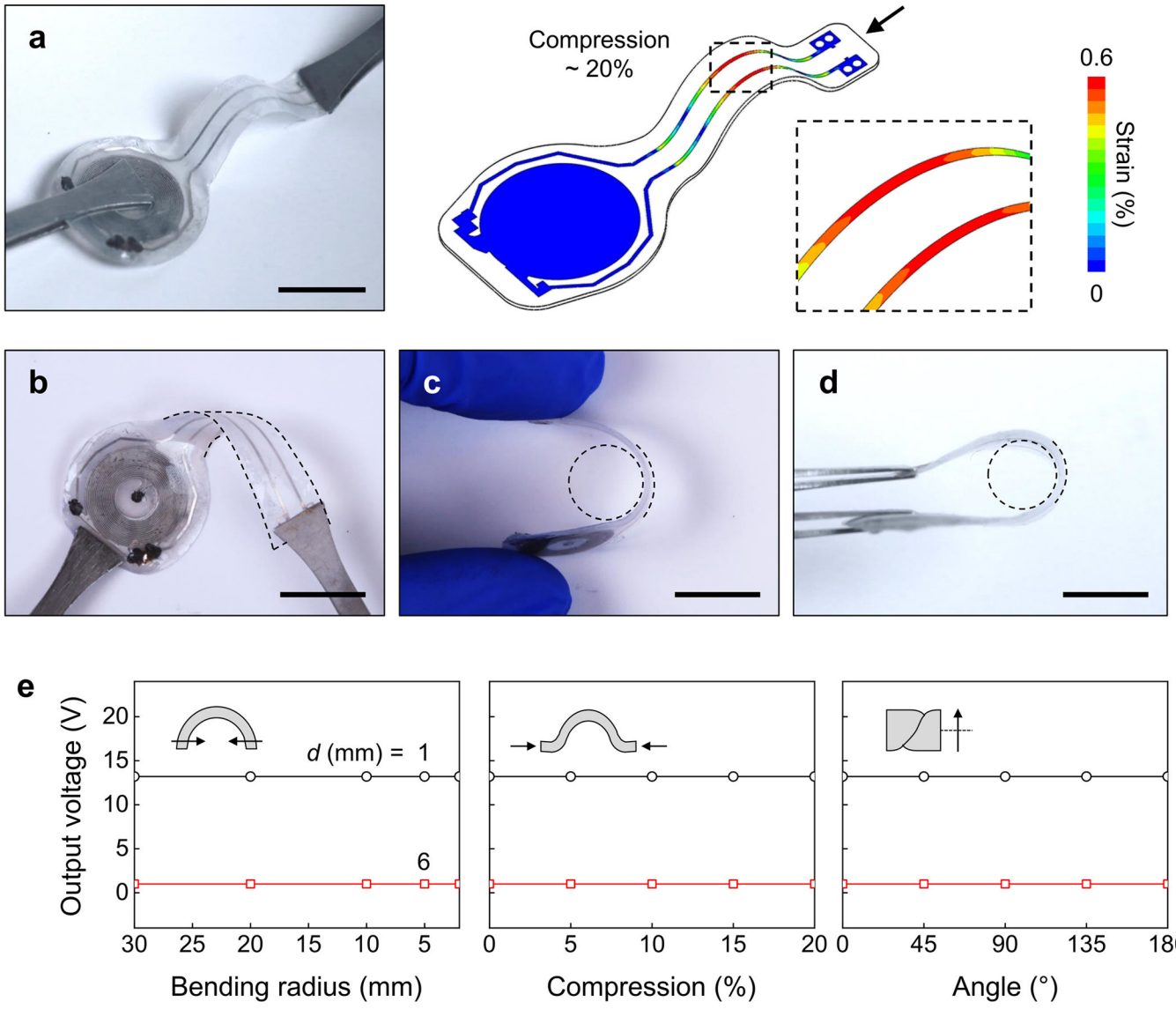

Extended Data Fig. 3 |. Modeling and experimental studies of mechanical reliability of the bioresorbable, leadless cardiac pacemaker.

a, Photograph (left) and FEA (right) results for devices during compressive buckling (20%). Scale bar, 10 mm. **b, c, d**, Photograph of twisted (180°) and bent (bend radius = 4 mm) devices. Scale bar, 10 mm. e, Output voltage of a device as a function of bending radius (left), compression (middle), and twist angle (right) at different distances between the Rx and Tx coils (black, 1 mm; red 6 mm). n = 3 independent samples.

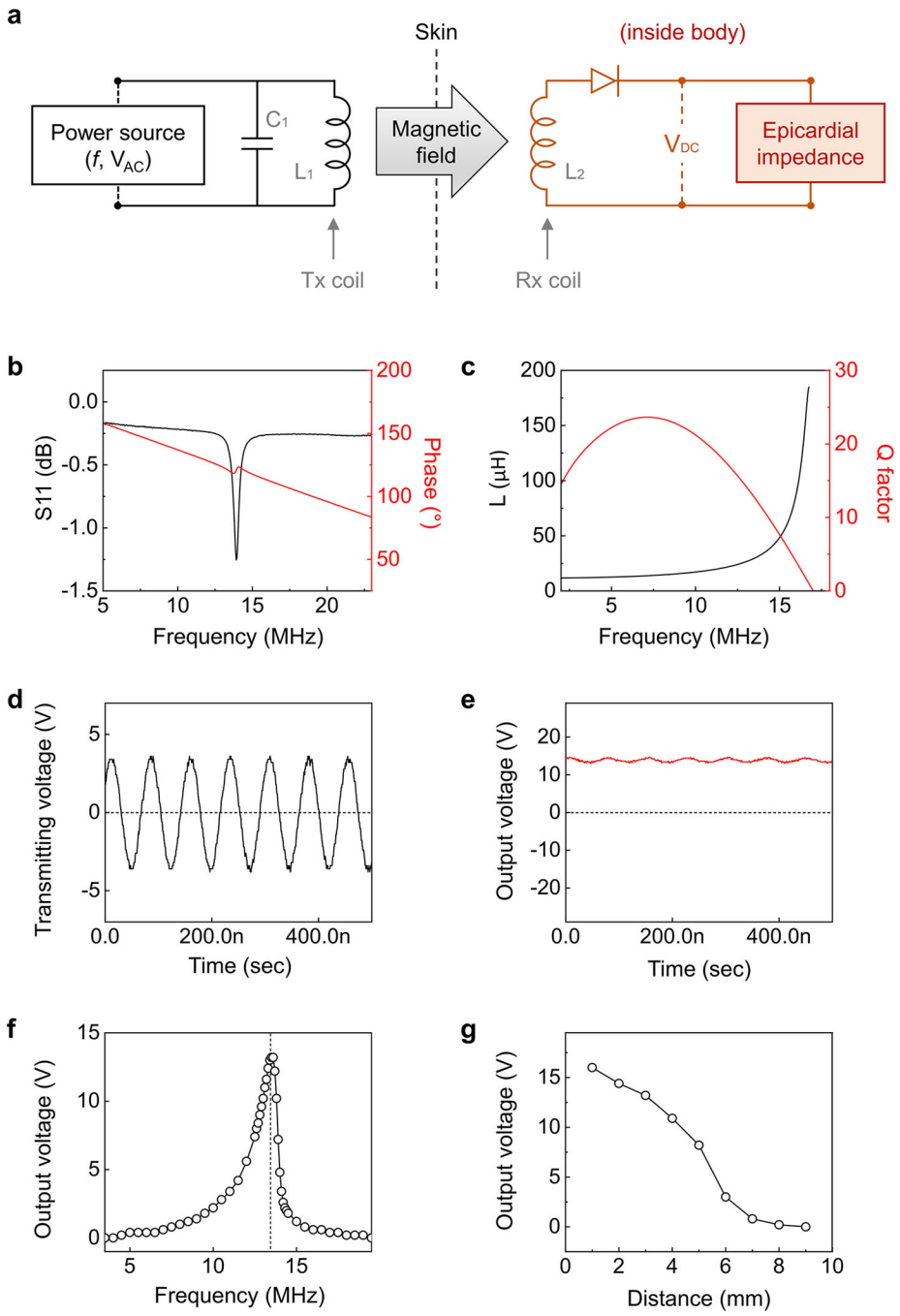

Extended Data Fig. 4 |. Electrical performance characteristics of the wireless power transfer system.

a, Schematic illustration of the circuit diagram for the transmission of RF power. Monophasic electrical pulses (programmed duration; alternative current) are generated by a waveform generator at ~13.5 MHz (Agilent 33250 A, Agilent Technologies, USA). The voltage can be further increased with an amplifier (210 L, Electronics & innovation, Ltd., USA). The generated waveforms (that is input power) are delivered to the Tx coil (3 turns, 20 mm diameter). This RF power is transferred to the Mg Rx coil (17 turns, 12 mm diameter) of an implanted bioresorbable cardiac pacemaker. The received waveform is

transformed into a direct current output via the RF diode to stimulate the targeted tissue. **b**, Measured RF behavior of the stimulator (black, S11; red, phase). The resonance frequency is ~13.5 MHz. **c**, Simulation results for inductance (L) and Q factor as a function of frequency. **d**, An alternating current (sine wave) applied to the Tx coil. The resonance frequency and input voltage (that is transmitting voltage) are ~13.5 MHz and 7 Vpp, respectively. **e**, Example direct current output of ~13.2 V wirelessly generated via the Rx coil of the bioresorbable device. **f**, Output voltage as a function of transmitting frequency. At the resonance frequency (~13.5 MHz) of the receiver coil (transmitting voltage = 7 V), the device produces a maximum output voltage of ~13.2 V. g, Output voltage as a function of the distance between the Tx and Rx coils (transmitting voltage = 10 Vpp; transmitting frequency = ~13.5 MHz).

Supplementary Material

Refer to Web version on PubMed Central for supplementary material.

Acknowledgements

This work made use of the NUFAB facility of Northwestern University's NUANCE Center, which has received support from the Soft and Hybrid Nanotechnology Experimental Resource (NSF no. ECCS-1542205); the MRSEC program (NSF no. DMR-1720139) at the Materials Research Center; the International Institute for Nanotechnology (IIN); the Keck Foundation; and the State of Illinois, through the IIN. This work was also performed in part at The George Washington University Nanofabrication and Imaging Center. We acknowledge support from the Leducq Foundation projects RHYTHM and R01-HL141470 (to I.R.E. and J.A.R.). R.T.Y. acknowledges support from the American Heart Association Predoctoral Fellowship (no. 19PRE34380781). R.A. acknowledges support from the National Science Foundation Graduate Research Fellowship (NSF no. 1842165) and the Ford Foundation Predoctoral Fellowship. Z.X. acknowledges the support from the National Natural Science Foundation of China (grant no. 12072057) and Fundamental Research Funds for the Central Universities (grant no. DUT20RC(3)032). B.P.K. and D.J. acknowledge support from a research donation by Mr and Mrs Ronald and JoAnne Willens. We thank NU Comprehensive Transplant Center Microsurgery Core for help with cardiac implantation surgical procedures. We also thank the Washington Regional Transplant Community, heart organ donors and families of the donors; our research would not have been possible without their generous donations and support.

Data availability

All data that support the findings of this study are included in the manuscript. Source data are provided with this paper.

References

1. Waldo AL, Wells JLJ, Cooper TB & MacLean WA Temporary cardiac pacing: applications and techniques in the treatment of cardiac arrhythmias. Prog. Cardiovasc. Dis. 23, 451–474 (1981). [PubMed: 7015414]
2. Zoll PM et al. External noninvasive temporary cardiac pacing: clinical trials. Circulation 71, 937–944 (1985). [PubMed: 3886190]
3. Curtis JJ et al. A critical look at temporary ventricular pacing following cardiac surgery. Surgery 82, 888–893 (1977). [PubMed: 303815]
4. Wilhelm MJ et al. Cardiac pacemaker infection: surgical management with and without extracorporeal circulation. Ann. Thorac. Surg. 64, 1707–1712 (1997). [PubMed: 9436559]
5. Choo MH et al. Permanent pacemaker infections: characterization and management. Am. J. Cardiol. 48, 559–564 (1981). [PubMed: 7270461]
6. Imparato AM & Kim GE Electrode complications in patients with permanent cardiac pacemakers. Arch. Surg. 105, 705–710 (1972). [PubMed: 5081544]

7. Bernstein V, Rotem CE & Peretz DI Permanent pacemakers: 8-year follow-up study. Incidence and management of congestive cardiac failure and perforations. Ann. Intern. Med. 74, 361–369 (1971). [PubMed: 5552109]
8. Hartstein AI, Jackson J & Gilbert DN Prophylactic antibiotics and the insertion of permanent transvenous cardiac pacemakers. J. Thorac. Cardiovasc. Surg. 75, 219–223 (1978). [PubMed: 625126]
9. Austin JL, Preis LK, Crampton RS, Beller GA & Martin RP Analysis of pacemaker malfunction and complications of temporary pacing in the coronary care unit. Am. J. Cardiol. 49, 301–306 (1982). [PubMed: 7058746]
10. Lumia FJ & Rios JC Temporary transvenous pacemaker therapy: an analysis of complications. Chest 64, 604–608 (1973). [PubMed: 4750332]
11. Donovan KD & Lee KY Indications for and complications of temporary transvenous cardiac pacing. Anaesth. Intensive Care 13, 63–70 (1985). [PubMed: 3977066]
12. Braun MU et al. Percutaneous lead implantation connected to an external device in stimulation-dependent patients with systemic infection – a prospective and controlled study. Pacing Clin. Electrophysiol. 29, 875–879 (2006). [PubMed: 16923004]
13. Del Nido P & Goldman BS Temporary epicardial pacing after open heart surgery: complications and prevention. J. Card. Surg. 4, 99–103 (1989). [PubMed: 2519988]
14. Elmistekawy E Safety of temporary pacemaker wires. Asian Cardiovasc. Thorac. Ann. 27, 341–346 (2019). [PubMed: 30776903]
15. Gutruf P et al. Wireless, battery-free, fully implantable multimodal and multisite pacemakers for applications in small animal models. Nat. Commun. 10, 5742 (2019). [PubMed: 31848334]
16. Koo J et al. Wireless bioresorbable electronic system enables sustained nonpharmacological neuroregenerative therapy. Nat. Med. 24, 1830–1836 (2018). [PubMed: 30297910]
17. Choi YS et al. Stretchable, dynamic covalent polymers for soft, long-lived bioresorbable electronic stimulators designed to facilitate neuromuscular regeneration. Nat. Commun. 11, 5990 (2020). [PubMed: 33239608]
18. Won SM et al. Natural wax for transient electronics. Adv. Funct. Mater. 28, 1801819 (2018).
19. Choi YS, Koo J & Rogers JA Inorganic materials for transient electronics in biomedical applications. MRS Bull. 45, 103–112 (2020).
20. Makadia HK & Siegel SJ Poly lactic-co-glycolic acid (PLGA) as biodegradable controlled drug delivery carrier. Polymers (Basel) 3, 1377–1397 (2011). [PubMed: 22577513]
21. Hwang SW et al. Dissolution chemistry and biocompatibility of single-crystalline silicon nanomembranes and associated materials for transient electronics. ACS Nano 8, 5843–5851 (2014). [PubMed: 24684516]
22. Yin L et al. Mechanisms for hydrolysis of silicon nanomembranes as used in bioresorbable electronics. Adv. Mater. 27, 1857–1864 (2015). [PubMed: 25626856]
23. Yin L et al. Dissolvable metals for transient electronics. Adv. Funct. Mater. 24, 645–658 (2014).
24. Length F Chemical and structural characterization of Candelilla (Euphorbia antisyphilitica Zucc.). J. Med. Plants Res. 7, 702–705 (2013).
25. Winter KF, Hartmann R & Klinke R A stimulator with wireless power and signal transmission for implantation in animal experiments and other applications. J. Neurosci. Methods 79, 79–85 (1998). [PubMed: 9531463]
26. Dinis H, Colmiais I & Mendes PM Extending the limits of wireless power transfer to miniaturized implantable electronic devices. Micromachines 8, 359 (2017).
27. Kang SK et al. Bioresorbable silicon electronic sensors for the brain. Nature 530, 71–76 (2016). [PubMed: 26779949]
28. Shreiner DP, Weisfeldt ML & Shock NW Effects of age, sex, and breeding status on the rat heart. Am. J. Physiol. Content 217, 176–180 (1969).
29. Mačianskienė R et al. Evaluation of excitation propagation in the rabbit heart: optical mapping and transmural microelectrode recordings. PLoS ONE 10, e0123050 (2015). [PubMed: 25881157]
30. Lee PT et al. Left ventricular wall thickness and the presence of asymmetric hypertrophy in healthy young army recruits. Circ. Cardiovasc. Imaging 6, 262–267 (2013). [PubMed: 23307776]

31. Schwartzman D, Chang I, Michele JJ, Mirotznik MS & Foster KR Electrical impedance properties of normal and chronically infarcted left ventricular myocardium. J. Interv. Card. Electrophysiol. 3, 213–224 (1999). [PubMed: 10490477]
32. Salazar Y, Bragos R, Casas O, Cinca J & Rosell J Transmural versus nontransmural in situ electrical impedance spectrum for healthy, ischemic, and healed myocardium. IEEE Trans. Biomed. Eng. 51, 1421–1427 (2004). [PubMed: 15311828]
33. Clauss S et al. Animal models of arrhythmia: classic electrophysiology to genetically modified large animals. Nat. Rev. Cardiol. 16, 457–475 (2019). [PubMed: 30894679]
34. Pichorim SF Design of circular and solenoid coils for maximum mutual inductance. In Proc.14th International Symposium on Biotelemetry 71–77 (Tectum, 1998).
35. Kurs A et al. Wireless power transfer via strongly coupled magnetic resonances. Science 317, 83–86 (2007). [PubMed: 17556549]
36. Rahko PS Evaluation of the skin-to-heart distance in the standing adult by two-dimensional echocardiography. J. Am. Soc. Echocardiogr. 21, 761–764 (2008). [PubMed: 18187292]
37. C95.1–2005 IEEE Standard for Safety Levels with Respect to Human Exposure to Radio Frequency Electromagnetic Fields, 3 kHz to 300 GHz (revision of IEEE Std C95.1–1991). 10.1109/IEEESTD.2006.99501 (2006).
38. Choi YS et al. Biodegradable polyanhydrides as encapsulation layers for transient electronics. Adv. Funct. Mater. 30, 2000941 (2020).
39. Koo J et al. Wirelessly controlled, bioresorbable drug delivery devices with active valves that exploit electrochemically triggered crevice corrosion. Sci. Adv. 6, eabb1093 (2020). [PubMed: 32923633]
40. Katsura M, Sato J, Akahane M, Kunimatsu A & Abe O Current and novel techniques for metal artifact reduction at CT: practical guide for radiologists. Radiographics 38, 450–461 (2018). [PubMed: 29528826]
41. Lee YK et al. Dissolution of monocrystalline silicon nanomembranes and their use as encapsulation layers and electrical interfaces in water-soluble electronics. ACS Nano 11, 12562–12572 (2017). [PubMed: 29178798]
42. Sofia SJ, Premnath V & Merrill EW Poly(ethylene oxide) grafted to silicon surfaces: grafting density and protein adsorption. Macromolecules 31, 5059–5070 (1998). [PubMed: 9680446]
43. Nakanishi K, Sakiyama T & Imamura K On the adsorption of proteins on solid surfaces, a common but very complicated phenomenon. J. Biosci. Bioeng. 91, 233–244 (2001). [PubMed: 16232982]
44. Lee G, Choi YS, Yoon H-J & Rogers JA Advances in physicochemically stimuli-responsive materials for on-demand transient electronic systems. Matter 3, 1031–1052 (2020).
45. Sperelakis N & Hoshiko T Electrical impedance of cardiac muscle. Circ. Res. 9, 1280–1283 (1961). [PubMed: 13915720]
46. Fry CH et al. Cytoplasm resistivity of mammalian atrial myocardium determined by dielectrophoresis and impedance methods. Biophys. J. 103, 2287–2294 (2012). [PubMed: 23283227]
47. Gabriel S, Lau RW & Gabriel C The dielectric properties of biological tissues: II. Measurements in the frequency range 10 Hz to 20 GHz. Phys. Med. Biol. 41, 2251–2269 (1996). [PubMed: 8938025]
48. Rong C et al. Analysis of wireless power transfer based on metamaterial using equivalent circuit. J. Eng. 2019, 2032–2035 (2019).
49. George SA, Brennan JA & Efimov IR Preclinical cardiac electrophysiology assessment by dual voltage and calcium optical mapping of human organotypic cardiac slices. J. Vis. Exp. 10.3791/60781 (2020).

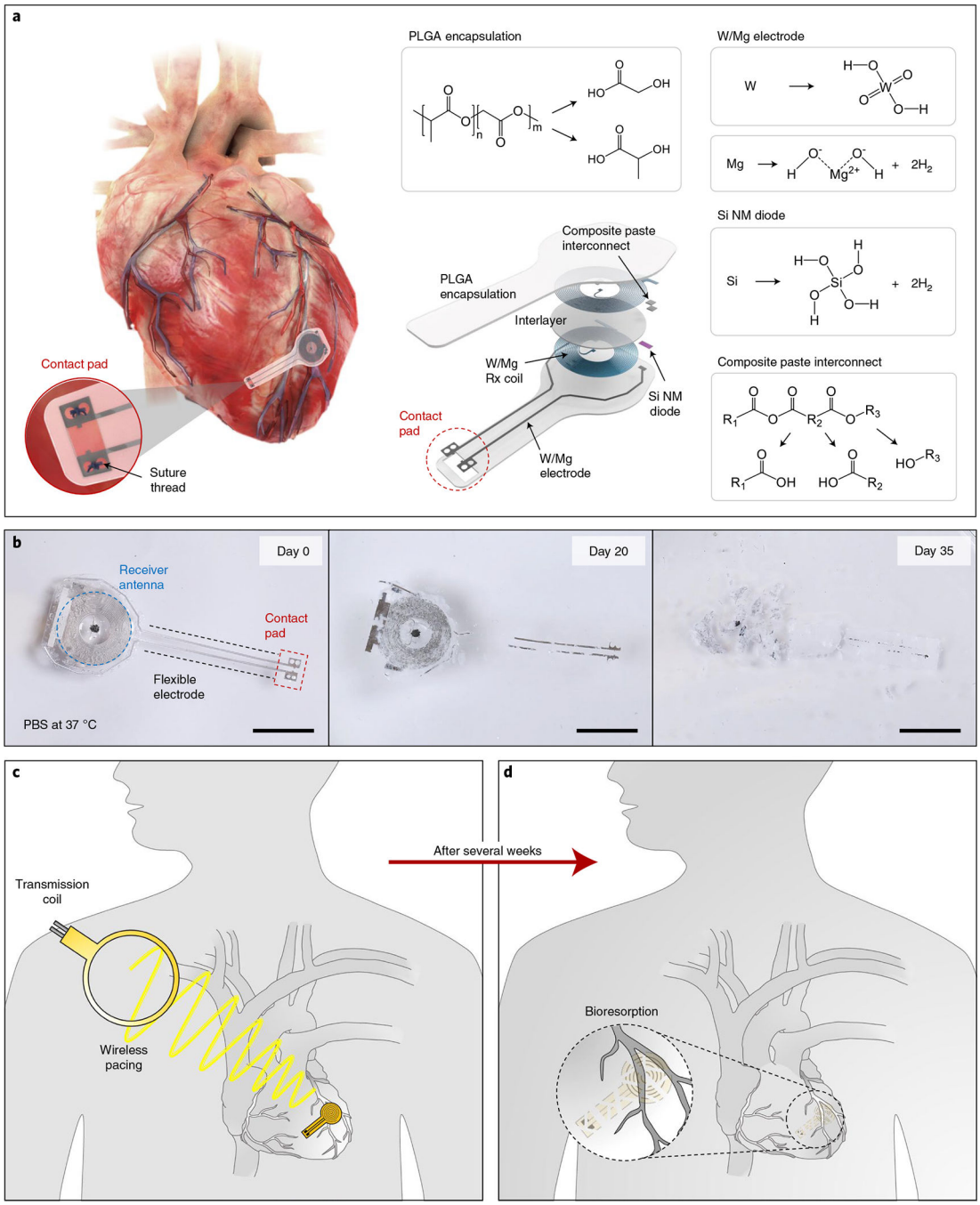

Fig. 1 |. Materials, design features and proposed utilization of a bioresorbable, implantable, leadless, battery-free cardiac pacemaker.

a, Left: schematic illustration of the device mounted on myocardial tissue. Middle: the electronic component is composed of three functional parts: (1) a wireless receiver, which consists of an inductive coil (W/Mg; thickness ~700 nm/~50 μm), a RF PIN diode (Si NM active layer, thickness 320 nm) and a dielectric interlayer (PLGA, thickness 50 μm) that acts as a power harvester and control interface; (2) flexible extension electrodes (W/Mg; thickness ~700 nm/~50 μm); and (3) a contact pad with exposed electrodes at the ends

to interface with myocardial tissue (inset). A composite paste of W microparticles in Candelilla wax serves as an electrical interconnection. The entire system, excluding the contact pad, rests between two encapsulation layers of PLGA (thickness ~100 μm). Right: all components of the device naturally bioresorb via hydrolysis and metabolic action in the body. PLGA degrades into its monomers, glycolic and lactic acid, and the W/Mg electrode degrades into WO_x and $Mg(OH)_2$, respectively; the Si NM degrades into nontoxic $Si(OH)_4$. Dissolution of Candelilla wax occurs by cleavage of the ester, anhydride and moieties via hydrolysis. **b**, Images of dissolution of a device associated with immersion in PBS (pH 7.4) at physiological temperature (37 °C). Scale bars, 10 mm. **c**, Schematic illustration of the wireless and battery-free operation of an implanted device via inductive coupling between an external transmission coil (Tx) and the receiver (Rx) coil on the device. **d**, Bioresorption subsequently eliminates the device after a period of therapy to bypass the need for device removal.

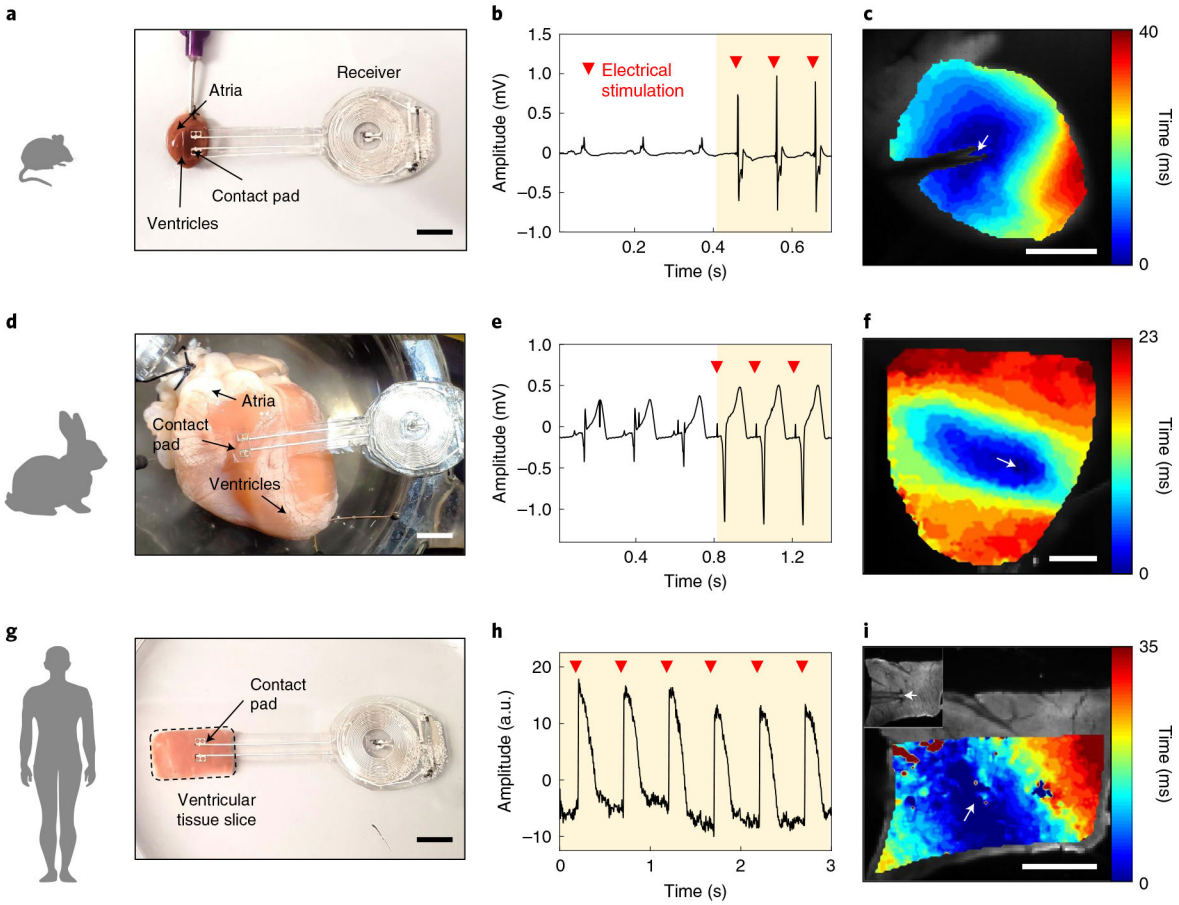

Fig. 2 |. Ex vivo demonstrations of bioresorbable cardiac pacemakers on mouse and rabbit hearts and human cardiac tissue.

a–g, Bioresorbable cardiac pacemakers. Images of mouse (**a**) and rabbit (**d**) hearts and a human ventricular cardiac tissue slice (**g**). Positioning of the electrode of the bioresorbable pacemaker on the anterior ventricular myocardium (**a,d**) and on the surface of the human ventricular cardiac tissue slice (**g**). Scale bars, 10 mm. **b**,**e**,**h**, Far-field ECG recordings (**b,e**) and optical action potential maps (**h**) before (plain background) and during (shaded background; red arrowheads indicate delivered electrical stimuli) electrical stimulation using bioresorbable pacemakers. **c**,**f**,**i**, Activation maps of membrane potential for mouse (**c**), rabbit (**f**) and human myocardium (**i**) showing activation originating from the location of the electrode pad of the device, as indicated by the white arrows. Scale bars, 5 mm.

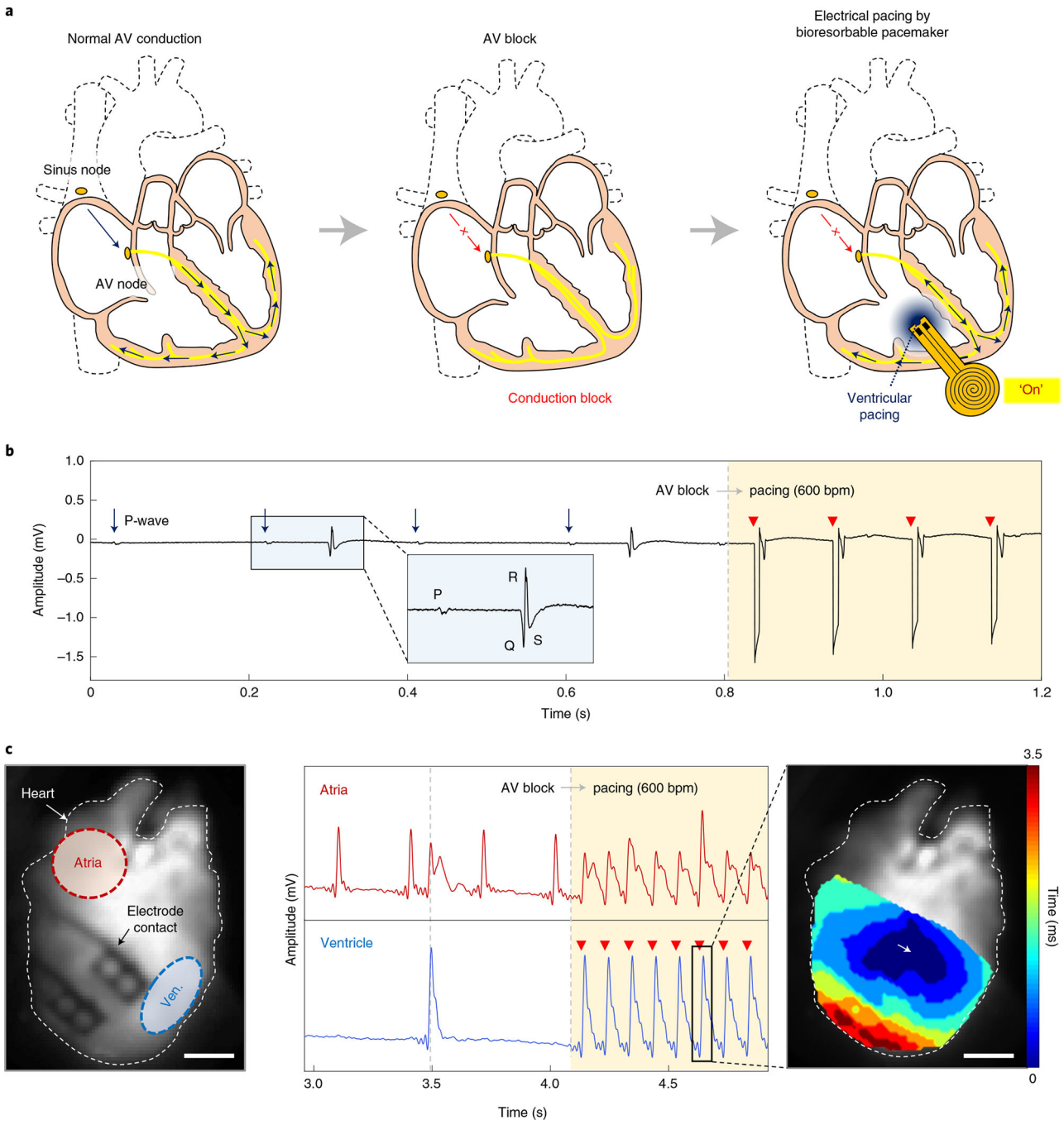

Fig. 3 |. Treatment of AV block using a bioresorbable, leadless cardiac pacemaker in an ex vivo Langendorff-perfused mouse model.

a, Schematic illustration of the nature of AV block and its treatment. In complete AV block, the conduction signal does not properly propagate from the atria to the ventricles. The pacemaker provides an electric impulse to restore activation of the ventricles.

b, Far-field ECG monitoring of a mouse heart with second-degree AV block (plain background). Ventricular capture via electrical stimulation using a bioresorbable device, as shown in the far-field ECG signal (shaded background; red arrowheads indicate delivered

electrical stimuli). Magnified insets illustrate a representative P-wave and QRS complex observed during second-degree AV block. **c**, Left: bright-field image of a mouse heart. The electrode of the bioresorbable pacemaker is positioned onto the anterior myocardial surface. Red and blue circles indicate the locations in the atria and ventricles (ven.), respectively, corresponding to the presented optical action potentials. Middle: simultaneous measurements of atrial and ventricular optical action potentials before stimulation (plain background) show asynchronous activation between the atria and ventricles indicating second-degree AV block. When electrical stimulation is delivered by the pacemaker (shaded background; red arrowheads indicate delivered electrical stimuli), the device restores activation of the ventricles. Right: activation map of the membrane potential during electrical stimulation by the device presents activation originating from the location of the contact pad, as indicated by the white arrow. Scale bars, 2 mm.

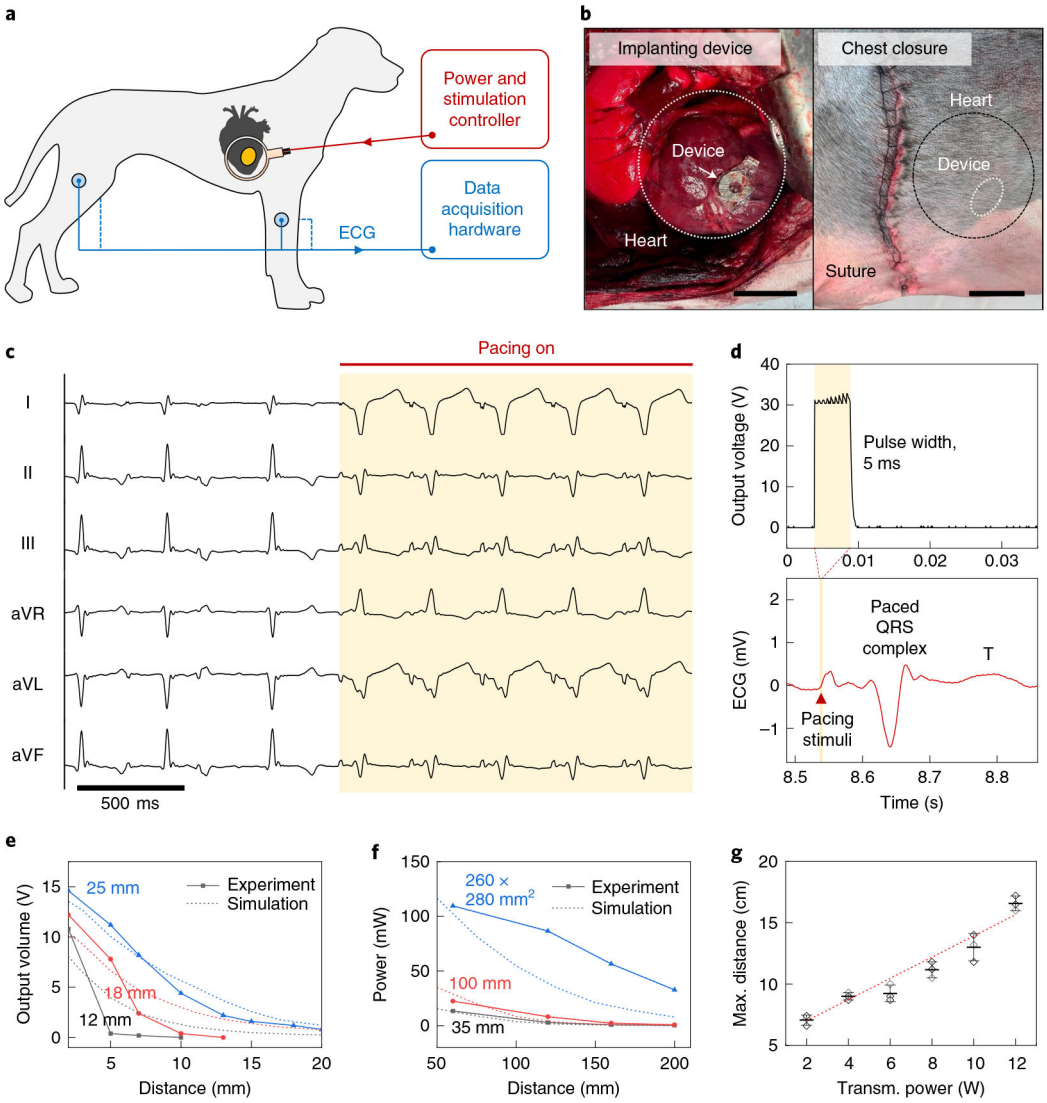

Fig. 4 |. Demonstration of a bioresorbable, leadless cardiac pacemaker in an in vivo canine model.

a, Schematic diagram of the test setup. **b**, Photographs of an open-chest procedure with the device sutured to the ventricular epicardium (left) and a sutured incision after chest closure (right). Scale bars, 5 cm. **c**, Six-lead ECG recording of intrinsic rhythm (plain background, ~120 bpm) and ventricular capture (shaded background, ~200 bpm) using the device. $n = 3$ biologically independent animals per group. **d**, Time dependence of the output voltage generated by the device (30 V, 5 ms) and corresponding ECG recordings from the canine heart. **e**, Output voltage as a function of the distance between the Rx and Tx coils (transmitting voltage, 3.6 V). Different colors indicate three different sizes of Rx coil: black, 12 mm; red, 18 mm; blue, 25 mm. **f**, Output power as a function of the distance between the Rx and Tx coils (diameter of Rx coil, 25 mm; input frequency, 13.56 MHz; input power, 12 W; load resistance, 5,000 Ω). Different colors indicate three different designs for the Tx coils: black (solenoid type, four turns, 35-mm diameter); red (solenoid type, four turns, 100-mm diameter); blue (square, one turn, 260 × 280 mm^2). **g**, In vivo closed chest canine

model studies of maximum pacing distance (that is, the greatest distance between the two coils that enables consistent ventricular capture) as a function of transmitted (transm.) power (input frequency, 13.56 MHz). The tests used Tx coils III (square, one turn, 260 × 280 mm^2) and an Rx coil with a diameter of 25 mm. $n = 3$ biologically independent animals per condition. **g**, Data are presented as mean ± s.e.m.

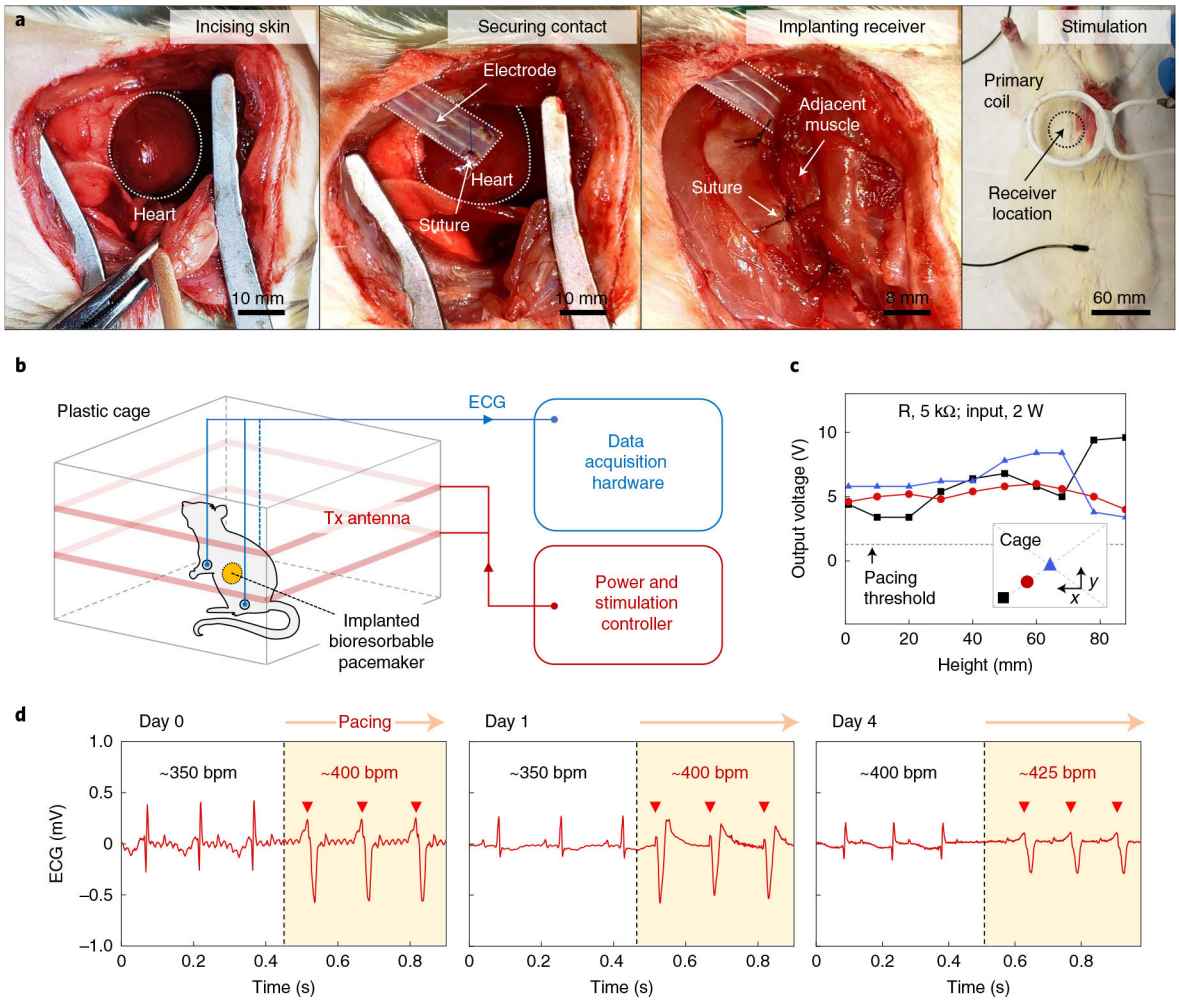

Fig. 5 |. Implantation and operation of a bioresorbable, leadless cardiac pacemaker in a chronic in vivo rat model.

a, Surgical procedure for implantion of the device. The electrodes laminate onto the surface of the cardiac tissue, where they are sutured onto the anterior left ventricular myocardium. A small primary coil facilitates rapid testing of the functionality of the device. **b**, Schematic diagram of a wireless pacing system setup that supports operation across a cage environment. **c**, Spatially resolved wireless output voltage in a cage with an RF power of 2 W applied to the coils around the perimeter of the cage (load resistance (R), 5 kΩ; input frequency, 13.56 MHz). The output voltage of the bioresorbable pacemaker exceeds a threshold of 1 V regardless of the height and position of the device. **d**, ECG signals before (plain background) and during electrical stimulation (shaded background; red arrowheads indicate delivered electrical stimuli) with the implanted bioresorbable cardiac pacemaker for 4 days. $n = 5$ biologically independent animals.

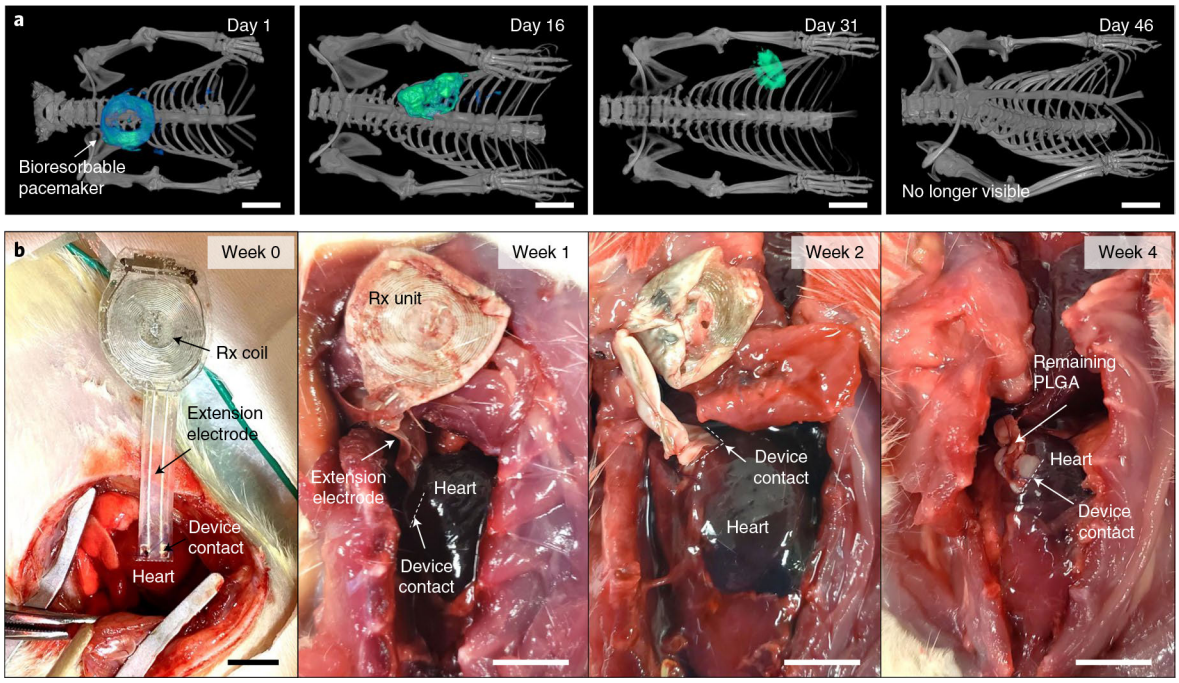

Fig. 6 |. Bioresorbability studies of the leadless cardiac pacemaker.

a, Three-dimensional-rendered CT images of rats collected over 7 weeks after the implantation of bioresorbable cardiac pacemakers. The images indicate the gradual disappearance of the devices to a stage where they are no longer visible on day 46. Scale bars, 10 mm. $n = 3$ biologically independent animals. **b**, Images of devices implanted in a rat model at different stages of bioresorption over the course of 4 weeks. The results reveal the mechanisms of bioresorption of the device after a therapeutic period. Scale bars, 5 mm. $n = 3$ biologically independent animals.

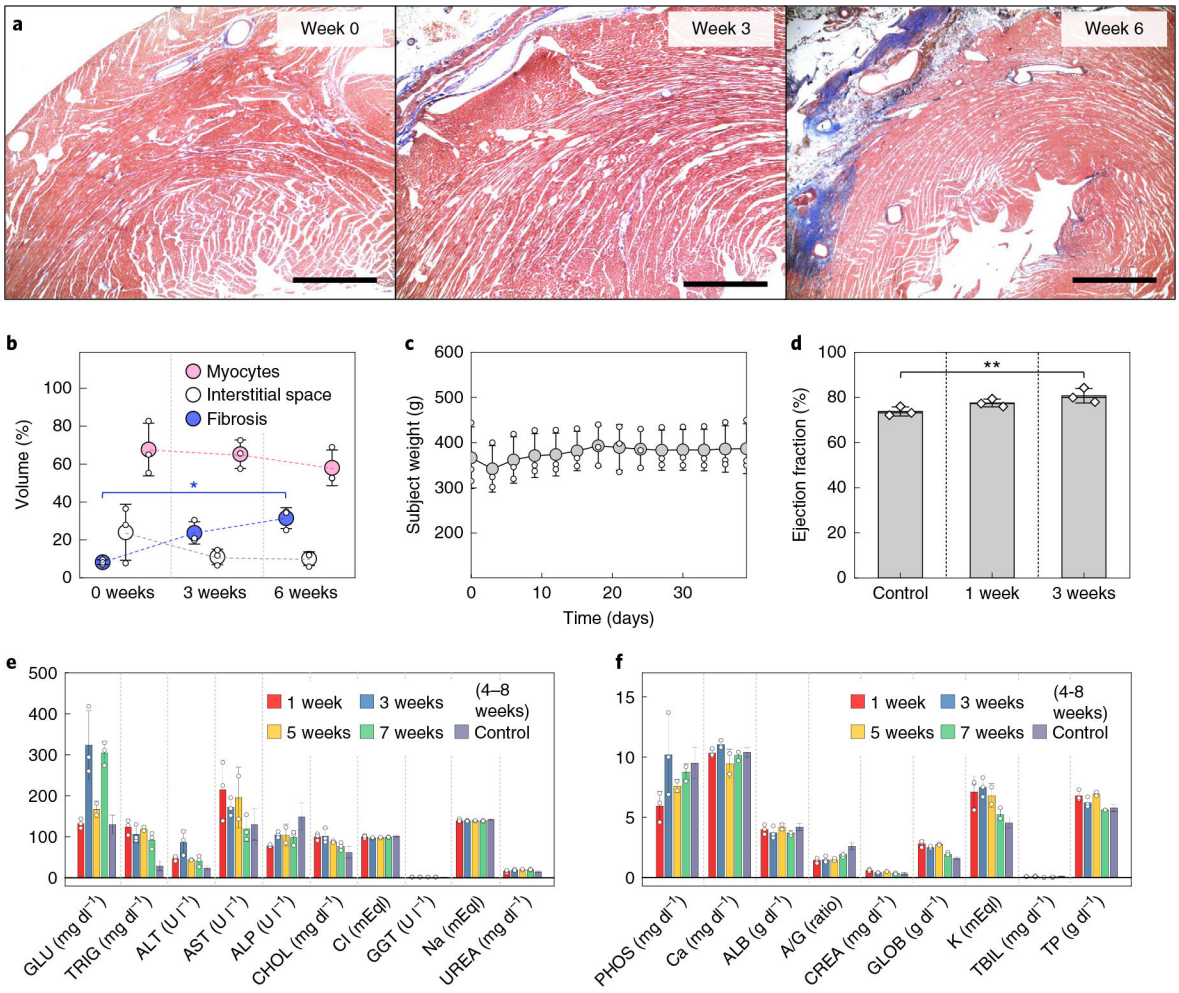

Fig. 7 |. Biocompatibility and toxicity studies of a bioresorbable, leadless cardiac pacemaker.

a, Representative image of Masson's trichrome staining of a cross-sectional area of the anterior left ventricle of a rat (left) without (0 weeks) and with an implanted device after (middle) 3 weeks and (right) 6 weeks near the site of implantation. $n = 3$ animals per group examined over three independent experiments. Scale bars, 1 mm. **b**, Percentage volume of myocytes (pink), interstitial space (white) and fibrosis (blue) in transmural cardiac cross-sections of rats without an implant, 3 weeks and 6 weeks following implantation. Kruskal–Wallis test: interstitial space: H(2), 0.08889, $P = 0.9929$; fibrosis: H(2), 6.489, $P = 0.0107$; myocytes: H(2), 5.956, $P = 0.0250$. Dunn's multiple comparison test at a significance level of 0.05, $P = 0.0338$. $n = 3$ biologically independent animals per group. **c**, Weights of animals measured every 3 days following surgery show an initial decrease, as anticipated after a major surgery, but increase appropriately with age, as expected in healthy animals. $n = 3$ biologically independent animals per group. **d**, Absence of significant changes in ejection fraction in rats before device implantation (control) and 1 and 3 weeks after implantation demonstrates the preservation of mechanical cardiac function (paired data; Friedman's test: $\chi^2_F(2) = 2.667$, $P = 0.3611$. Dunn's multiple comparison test at a significance level of 0.05). $n = 3$ biologically independent animals. **e,f**, Analysis of complete blood counts and blood chemistry for rats with and without device implantation reveals maintenance of overall

healthy physiology in the animals. $n = 3$ biologically independent animals. Control data were provided by Charles River Laboratories. GLU, glucose; TRIG, triglycerides; ALT, alanine aminotransferase; AST, aspartate transaminase, ALP, alkaline phosphatase; CHOL, cholesterol; Cl, chloride; GGT, gamma-glutamyl transferase; Na, sodium; UREA, urea; PHOS, phosphorus; Ca, calcium; ALB, albumin; A/G, albumin/globulin; CREA, creatinine; GLOB, globulin; K, potassium; TBIL, total bilirubin; TP, total protein. **b–f**, Data are presented with error bars as means ± s.d.